

A Coupled Ground Heat Flux-Surface Energy Balance Model of Evaporation Using Thermal Remote Sensing Observations

Bimal K. Bhattacharya^{1*}, Kaniska Mallick^{2,3*}, Devansh Desai^{1,10,11}, Ganapati S. Bhat⁴, Ross Morrison⁵, Jamie Clevery⁶, Will Woodgate⁷, Jason Beringer⁸, Kerry Cawse-Nicholson⁹, Siyan Ma³, Joseph Verfaillie³, Dennis Baldocchi³

¹Agriculture & Land Ecosystem Division, Space Applications Center, ISRO, Ahmedabad, India

²Remote Sensing and Natural Resources Modeling, Department ERIN, Luxembourg Institute of Science and Technology, Belvaux, Luxembourg

³Environmental Science Policy and Management, University of California, Berkeley, United States

⁴Centre for Atmosphere and Oceanic Studies, Indian Institute of Sciences, Bengaluru, India

⁵Centre for Ecology and Hydrology, Lancaster, UK

⁶Terrestrial Ecosystem Research Network, College of Science and Engineering, James Cook University, Cairns, Queensland

⁷CSIRO Land and Water, Private Bag 5, Floreat 6913, Western Australia.

⁸School of Earth and Environment, The University of Western Australia, WA, 6009, Australia

⁹Carbon Cycles and Ecosystems, Jet Propulsion Laboratory, California Institute of Technology, United States

¹⁰Department of Physics, Electronics & Space Sciences, Gujarat University, Ahmedabad, India

¹¹Department of Physics, Institute of Science, Silver Oak University, Ahmedabad, Gujarat, India

Corresponding authors: Bimal K. Bhattacharya (bkbhattacharya@sac.isro.gov.in) and Kaniska Mallick (kaniska.mallick@gmail.com)

29 **Abstract**

30 One of the major undetermined problems in evaporation (ET) retrieval using thermal infrared
31 remote sensing is the lack of a physically based ground heat flux (G) model and its integration
32 with in the surface energy balance (SEB) ~~model equation~~. Here, we present a novel approach based
33 on coupling a thermal inertia (TI)-based mechanistic G model with an analytical surface energy
34 balance model, Surface Temperature Initiated Closure (STIC, version STIC1.2). The coupled
35 model is named STIC-TI, ~~and it uses~~ The model is driven by noon-night (1:30 pm and am) land
36 surface temperature, surface albedo, and vegetation index from MODIS Aqua in conjunction with
37 a clear-sky net radiation sub-model and ancillary meteorological information. SEB flux estimates
38 from STIC-TI were evaluated with respect to the *in-situ* fluxes from ~~Eddy-eddy Covariance~~
39 covariance measurements in diverse ecosystems of contrasting aridity in both northern and
40 southern hemispheres. Sensitivity analysis revealed substantial sensitivity of STIC-TI-derived
41 fluxes due to the land surface temperature uncertainty. An evaluation of noontime G (G_i) estimates
42 showed 12 – 21% error across six flux tower sites ~~in both the hemispheres~~ and a comparison
43 between STIC-TI versus ~~other empirical~~ G models also revealed the substantially better
44 performance of the former. While the instantaneous noontime net radiation (R_{Ni}) and latent heat
45 flux (LE_i) ~~was were~~ overestimated (15% and 25%), sensible heat flux (H_i) was underestimated
46 (22%). ~~The errors in G_i were associated with the errors in daytime T_s and mismatch of footprint~~
47 ~~between the model estimates and measurements~~. Overestimation (underestimation) of LE_i (H_i) was
48 associated with the overestimation of net available energy ($R_{Ni} - G_i$) and use of unclosed surface
49 energy balance SEB flux measurements in LE_i (H_i) validation. The mean percent deviations in G_i
50 and H_i estimates were found to be strongly correlated with satellite day-night view angle difference
51 in parabolic and linear pattern, and a relatively weak correlation was found between day-night
52 view angle difference versus LE_i deviation. Findings from this parameter-sparse coupled G-ET
53 model ~~Being independent of any leaf-scale parameterization and having a coupled sub-model of~~
54 G, STIC-TI can make a valuable contribution to mapping and monitoring the spatiotemporal
55 variability of ecosystem water stress and evaporation using noon-night thermal infrared
56 observations from ~~existing and~~ future Earth Observation satellite missions such as INSAT-4th
57 generation and TRISHNA, LSTM, and SBG.

58 **Keywords:** Thermal remote sensing, water stress, evaporation, ground heat flux, thermal inertia,
59 surface energy balance, STIC, terrestrial ecosystem

60 1 Introduction

61 One of the outstanding challenges in evaporation (ET) estimation through surface energy balance
62 (SEB) model concerns an accurate characterization of ground heat flux in the open canopy ~~system~~
63 ~~architecture~~ with mixed vegetation such as savanna or in ecosystems with low mean fractional
64 vegetation cover, prevailing water stress, and strong seasonality in soil moisture. Ground heat flux
65 (G) is an intrinsic component of SEB (Sauer and Horton, 2005), affecting the net available energy
66 for ET (the equivalent water depth of latent heat flux, LE) and sensible heat flux (H). It represents
67 an energy flow path that couples surface with the atmosphere and has important implications for
68 the underlying thermal regime (Sauer and Horton, 2005). Depending on the vegetation fraction
69 and water stress, the magnitude of instantaneous G varies greatly across different ecosystems. In
70 the humid ecosystems with predominantly dense canopies and high mean fractional vegetation
71 cover, G contributes to a small proportion in the surface energy balance. Dense canopy cover leads
72 to less transmission of radiative fluxes through multiple layers of canopies, which results in low
73 warming of the soil floor. Due to persistently high soil water content, humid ecosystems generally
74 show low diurnal and seasonal variability in G. ~~By~~In contrast, the magnitude of G is substantially
75 large in arid and semi-arid ecosystems with sparse and open canopy and soil moisture deficits. Due
76 to prevailing feedback between the physics of ground heat flux, land-atmosphere interactions and
77 vegetation ecophysiology, evaporation modelling in the complex ecosystems ~~remained~~remains a
78 challenging task (Wang et al., 2013; Kiptala et al., 2013). This paper addresses the challenge of
79 simultaneous estimation of G and ET by combining thermal remote sensing observations with a
80 mechanistic G model and a SEB model.

81 SEB models mainly emphasize on estimating sensible heat flux (H) by resolving the aerodynamic
82 conductance (g_A) and computes LE as a residual SEB component as follows:

$$LE = R_N - G - H \quad (1)$$

83 R_N is the net radiation. The proportion of R_N that is partitioned into G depends upon soil properties
84 like its albedo, soil moisture, soil thermal properties such as thermal conductivity and heat
85 capacity, which vary with mineral, organic and soil water fractions. SEB models use land surface
86 temperature (LST or T_S) as an important lower boundary condition for estimating H and LE. Due
87 to the extraordinarily high sensitivity of T_S to evaporative cooling and soil water content variations,

88 thermal infrared (TIR) remote sensing is extensively used in large scale evaporation diagnostics
89 (Kustas and Anderson, 2009; Mallick et al., 2014, 2015a, 2018a; Cammalleri and Vogt, 2015;
90 Anderson et al., 2012). Evaporation estimation through SEB models commonly employ empirical
91 sub-models of G in a stand-alone mode. Despite the utility of mechanistic G models is
92 demonstrated in different studies (Verhoef, 2004; Murray and Verhoef, 2007; Verhoef et al.,
93 2012), no TIR-based evaporation study attempted to couple a mechanistic G model with a SEB
94 model.

95 The SEB models for ET estimation driven by remote sensing observations generally use linear and
96 non-linear relationships for estimating G and such methods generally employ R_N , T_S , albedo (α_R),
97 and NDVI (e.g., Bastiaanssen et al., 1998; Friedl, 2002; Santanello and Friedl, 2003). While the
98 inclusion of T_S and albedo serves as a proxy for soil moisture and surface characteristics effects in
99 G , inclusion of NDVI provides a scaling of $G - R_N$ ratio for different fractional vegetation cover.
100 Unfortunately, the empirical approaches do not include any information of soil temperature or
101 daily temperature amplitude. These empirical models also lack the universal consensus. Setting G
102 as a fraction of R_N does not solve the energy balance equation and disregards the role of thermal
103 inertia of the land surface (Mallick et al., 2015b). This could introduce substantial uncertainty in
104 LE estimation because G effectively couples the surface energy balance with energy transfer
105 processes in the soil thermal regime. It provides physical feedback to LE through the effects of
106 soil moisture, temperature, and conductivity (thermal and hydraulic) (Sauer and Horton, 2005).
107 Such feedbacks are most critical in the arid and semi-arid ecosystems where LE is significantly
108 constrained by the soil moisture dry-down. The limits imposed on LE by the water stress
109 consequently result in greater partitioning of the net available energy (i.e., $R_N - G$) into H and G
110 (Castelli et al., 1999).

111 When LE is reduced due to soil moisture dry-down, both G and T_S tend to show rapid intra-
112 seasonal rise. Therefore, the surface energy balance equation could be linked with mechanistic G
113 model, T_S harmonics (Verhoef, 2004), and soil moisture availability. Realizing the importance of
114 direct estimates of G in LE and invigorated by the advent of TIR remote sensing, Verhoef et al.
115 (2012) demonstrated the potential of a TI-based mechanistic model (Murray and Verhoef, 2007)
116 (MV2007 hereafter) for spatiotemporal G estimates in semi-arid ecosystems of Africa. Some
117 studies also emphasized the importance of using noontime and nighttime T_S and R_N for estimating

118 G (Mallick et al., 2015b; Bennet et al., 2008; Tsuang, 2005). The method of MV2007 has so far
119 been tested in a stand-alone mode, and no remote sensing method has so far been attempted to
120 combine such a mechanistic G model (e.g., MV2007-TI model) with a SEB model for coupled
121 energy-water flux estimation and validation.

122 By integrating T_s into a combined structure of the Penman-Monteith (PM) and Shuttleworth-
123 Wallace (SW) model, an analytical SEB model was proposed by Mallick et al. (2014, 2015a,
124 2016). The model, Surface Temperature Initiated Closure (STIC), is based on finding analytical
125 solution for aerodynamic and canopy-surface conductance (g_A and g_S) where the expressions of
126 the conductances were constrained by an aggregated water stress factor. Through physically
127 linking water stress (T_s derived) with g_A and g_S , STIC established direct feedback between T_s , H
128 and LE, and simultaneously overcame the need of empirical parameterization for estimating the
129 conductances (Mallick et al., 2016, 2018a). Different versions of STIC have been extensively
130 validated in different ecological transects (Tropical rainforest to woody savanna) and aridity
131 gradients (humid to arid) (Trebs et al., 2021; Bai et al., 2021; Mallick et al., 2015a; 2016; 2018a,
132 b; Bhattarai et al., 2018, 2019). Based on the conclusions of Verhoef et al. (2012), Mallick et al.
133 (2014; 2015a,b; 2016; 2018a,b, 2022), Bhattarai et al. (2018, 2019), and Bai et al. (2021), there is
134 a need to address some of the challenges in SEB modeling, which are, (i) accurate estimation of G
135 and ET in sparse vegetation, (ii) testing the utility of coupling a TI-based G model with an
136 analytical SEB model for accurately estimating G and ET, and (iii) detailed evaluation of a coupled
137 G-SEB model at the ecosystem scale. Realizing the significance of mechanistic G model
138 (MV2007), the advantage of the analytical STIC model, and to mitigate some of the overarching
139 gaps in SEB modeling in sparsely vegetated open canopy systems, this study presents the first-
140 ever coupled implementation of MV2007 G with the most recent version of STIC (STIC1.2). We
141 name this new coupled model as STIC-TI and it requires noon-night T_s and associated remotely
142 sensed land surface variables as inputs. We performed subsequent evaluation of STIC-TI in nine
143 terrestrial ecosystems in arid, semi-arid and sub-humid climate in India, the United States of
144 America (USA) (~~representing~~—northern hemisphere) and Australia (~~representing~~—southern
145 hemisphere) at the eddy covariance flux tower sites. The current study addresses the following
146 research questions and objectives:

147 (i) What is the performance of STIC-TI G estimates when compared with conventionally used
148 empirical G models in ecosystems having low mean fractional vegetation cover (f_c) (≤ 0.5) and
149 having larger soil exposure to radiation for example in Savanna?

150 (ii) How do the estimates from STIC-TI LE and H fluxes compare with LE and H observations in
151 diverse terrestrial ecosystems that represent a varied range of f_c (0.25 – 0.5) covering cropland,
152 savanna, mulga vegetation (woodlands and open-forests dominated by the mulga tree [*Acacia*
153 *aneura*]) spread across arid, semi-arid, sub-humid, humid climates over a vast range of rainfall
154 (250 to 1730 mm), temperature (-4 to 46°C) and soil regimes?

155 (iii) What is the seasonal variability of G and evaporative fraction from STIC-TI model in a wide
156 range of ecosystems having contrasting aridity and vegetation cover?

157 It is important to mention that assessing the performance of STIC-TI LE and H with respect to
158 other SEB models is not within the scope of the present study. The prime focus of the current study
159 is to assess the sensitivity of STIC-TI, temporal variability of the retrieved SEB fluxes, and cross-
160 site validation of the individual SEB components.

161 A list of variables, their symbols and corresponding units are given in Table A1 in Appendix A.

162 **2 Study area and datasets**

163 **2.1 Study site characteristics**

164 The present study was conducted using data from nine flux tower sites (four sites in India; three
165 sites in Australia; two sites in USA) equipped with Eddy Covariance (EC) measurement systems.

166 The distribution of the flux tower sites considered for the present study are shown in Fig.1 below.

167 The sites cover a wide range of climate, vegetation types, low fractional vegetation cover (f_c) of
168 around 0.5 and have contrasting aridity (Table 1). In India, a network of EC towers was set up

169 under Indo-UK INCOMPASS (INteraction of Convective Organization and Monsoon
170 Precipitation, Atmosphere, Surface and Sea) Program (Turner et al., 2019) at Jaisalmer (IND-Jai)

171 in Rajasthan state, Nawagam (IND-Naw) in Gujarat state, Samastipur (IND-Sam) in Bihar state
172 and under Newton-Bhaba programme (Morisson et al., 2019 a,b) at Dharwad (IND-Dha) in

173 Karnataka state. The flux footprint for EC towers in India varied from 500 m – 1 km (Bhat et al.,
174 2019). In the present study, about 90% of the fluxes came from an area within 500 m to 1 km from

175 the EC tower. Therefore, the relative contribution of vegetated land surface area to the fluxes is
 176 close to 90% (Schmid, 2002; Vesala et al., 2008). The remaining percentage of fluxes were
 177 originated from an area beyond the flux footprint. The mean annual f_c was found to vary from 0.25
 178 to 0.52 with standard deviation (SD) ranging from 0.1 to 0.16.

179 The IND-Jai site represents arid western zone over desert plains of natural grassland ecosystem.
 180 The region receives very low rainfall (100 – 300 mm) during monsoon and experiences a wide
 181 range in air temperature, high solar radiation, wind speed and high evaporative demand (Raja et
 182 al., 2015). The IND-Naw site represents semi-arid agroecosystem in the middle Gujarat
 183 agroclimatic zone of north-west India and has a pre-dominant rice-wheat cropping system. The
 184 IND-Sam site has sub-humid climate of north-west alluvial plain zone in the Indo-Gangetic Plain
 185 (IGP) situated in the eastern India and this site also follows rice-wheat crop rotation. IND-Dha
 186 represents humid sub-tropical climate of transition zone in the southern India and this site
 187 comprises of crops.

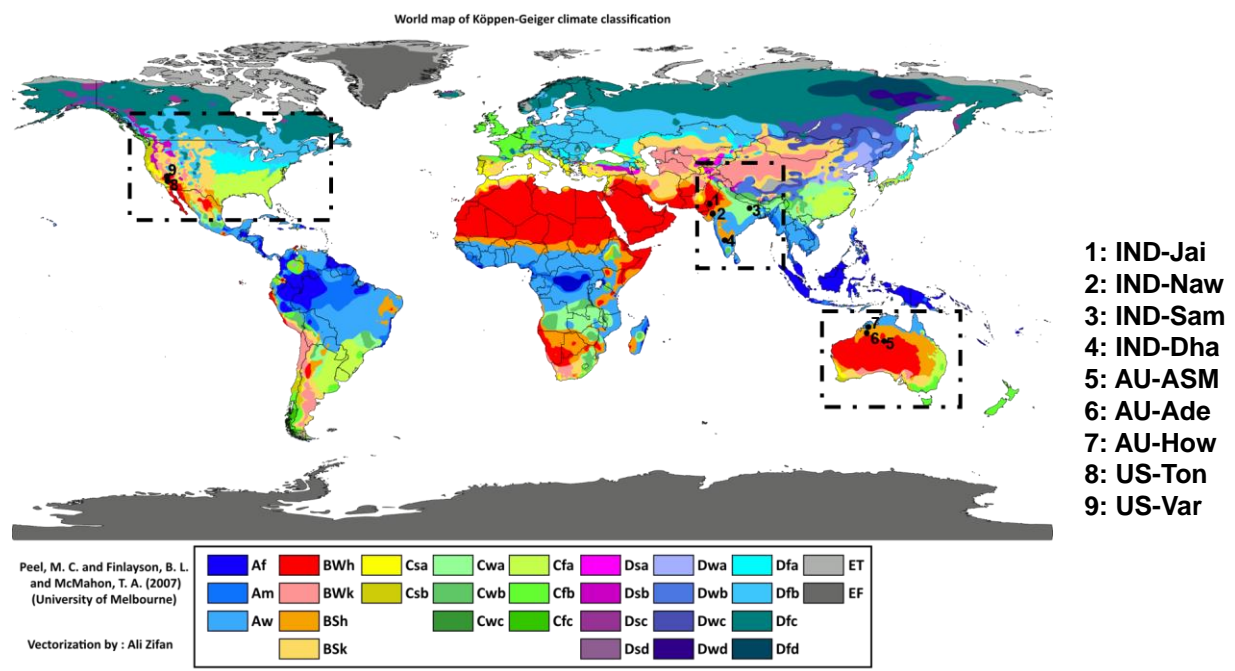


Figure 1: Locations of the flux tower sites in India, Australia and USA overlaid on climate type map. (Image Source: By Peel, M. C., Finlayson, B. L., and McMahon, T. A. (University of Melbourne) enhanced, modified, and vectorized by Ali Zifan; Hydrology and Earth System Sciences: "Updated world map of the Köppen-Geiger climate classification". Legend explanation, CC BY-SA 4.0, <https://commons.wikimedia.org/w/index.php?curid=47086879>)

188 In USA, two EC tower sites were located at Tonzi Ranch (US-Ton) and Vaira Ranch (US-Var), in
189 the lower foothills of the Sierra Nevada Mountains. Both the EC stations are part of the
190 AMERIFLUX Management Project (<https://ameriflux.lbl.gov/>). US-Ton is classified as an oak
191 savanna woodland. While the overstorey is dominated by blue oak trees (40% of total vegetation)
192 with intermittent grey pine trees (3 trees ~~per hectare~~^{ha⁻¹}), the understory species include a variety
193 of grasses and herbs. The mean annual rainfall at this site is 559 mm. US-Var is a grassland
194 dominated site and the growing season is confined to the wet season only, typically from October
195 to early May. The mean annual rainfall at this site is 559 mm. The mean annual f_c was found to
196 vary from 0.18 to 0.26 and SD of the order of 0.06 to 0.07.

197 In Australia, three EC tower sites were located at Howard Springs (AU-How), Alice Springs Mulga
198 (AU-ASM), Adelaide river (AU-Ade) in the Northern Territory as part of the OzFlux network
199 (Beringer et al., 2016) and the Terrestrial Ecosystem Research Network (TERN), which is
200 supported by the National Collaborative Infrastructure Strategy (NCRIS)
201 (<http://www.ozflux.org.au/monitoringsites/index.html>). The AU-How is situated in the Black
202 Jungle Conservation Reserve representing an open woodland savanna and the mean annual rainfall
203 is 1750 mm. The AU-ASM is located on Pine Hill cattle station near Alice Springs. The woodland
204 is characterized by mulga canopy and mean annual rainfall is 306 mm. AU-Ade represents savanna
205 with a mean annual rainfall of 1730 mm. The mean annual f_c varied from 0.21 to 0.48 having SD
206 range of 0.08 - 0.17. A description of Australian flux sites is given in Beringer et al. (2016).
207 Average heights of vegetation are 1.15 m at IND-Naw, 1 m at IND-Jai, 1.23 m at IND-Sam, 1.5
208 m at IND-Dha, 6.5 m at AU-ASM, 15m at AU-How, 7 m at AU-Ade, 10 m at US-Ton, and ≤ 0.5
209 m at US-Var.

210

211

212

213

214

215

216

217

218

219 **Table 1:** An overview of the EC flux tower site characteristics in the present study

Hemisphere	Sites	Latitude (°N), Longitude (°E)	Climate & Vegetation	Mean f_c (SD)	Soil texture	T_A range (°C)	Mean Annual P (mm)	Observation period
Northern	Jaisalmer (IND-Jai)	26.99, 71.34	Arid grassland	0.25(±0.1)	Loamy fine sand to coarse sand	8 – 40	250	2017 – 2018
	Nawagam (IND-Naw)	22.80, 72.57	Semi-arid cropland	0.41(±0.13)	Sandy loam	9 – 39	700	2017 – 2018
	Samastipur (IND-Sam)	26.00, 85.67	Humid subtropical cropland	0.52(±0.16)	Sandy loam to loam	10 – 39	1000	2017 – 2018
	Dharwad (IND-Dha)	15.50, 74.99	Tropical Savanna	0.36(±0.11)	Shallow to medium black clay and red sandy loam soils	12 – 40	650	2016 – 2018
	Tonzi ranch (US-Ton)	38.43, -120.96	Woody Savanna	0.18(±0.06)	Red sandy clay loam	0 – 40	559	2011 – 2019
	Vaira ranch (US-Var)	38.41, -120.95	Arid grassland	0.26(±0.07)	Rocky silt loam	0 – 40	559	2011 – 2019
Southern	Alice Springs Mulga (AU-ASM)	-22.28, 133.24	Semi-arid mulga	0.21(±0.09)	Loamy sand	(-4) – 40	305	2011 – 2014
	Howard Springs (AU-How)	-12.49, 131.15	Tropical savanna	0.48(±0.17)	Red kandasol	19 – 34	1700	2011 – 2014
	Adelaide River (AU-Ade)	-13.07, 131.11	Savanna	0.42(±0.08)	Yellow hydrosol, shallow, loamy sand with coarse gravel	16 – 37	1730	2007 – 2009

220 T_A : Air temperature during the observation period; P: rainfall (mm) measured using rain gauge at flux tower site during the study
 221 period. IND is for India, AU is for Australia, and US is for the United States; SD is standard deviation of annual mean f_c which is
 222 computed from NDVI as mentioned in section 3.1.

223 2.2 Datasets

224 2.2.1 Micrometeorological data at flux tower sites

225 Standardized, controlled and harmonized surface energy balance (SEB) flux and meteorological
226 data from nine EC towers were used in the present analysis. In Australia, H and LE were measured
227 through the EC systems and R_N were measured through net radiometers at varying heights of 15
228 m (AU-Ade), 23 m (AU-How), and 11.6 m (AU-ASM), respectively. In India, the EC
229 measurement height was maintained approximately at 8 m above the surface, except at IND-Dha
230 where it was installed at a height of 4.2 m. In USA, the SEB measurements were carried out at
231 tower heights of 23 m at US-Ton and 2 m US-Var. A summary of the instrumentation is given in
232 Table A2 of Appendix A. All the flux tower sites were equipped with a range of meteorological
233 instrumentation which measured diurnal air temperature (T_A) and relative humidity (R_H), four
234 components of the net radiation (R_N , consisting of down- and up-welling shortwave and long-wave
235 radiation (SW_{\downarrow} , SW_{\uparrow} , LW_{\uparrow} and LW_{\downarrow} , respectively)) above the vegetated canopy. In addition, the
236 diurnal soil heat flux (G) and soil temperature (T_{ST}) were measured at all the three Australian sites
237 and two US sites. In India, the diurnal soil heat flux was measured only at IND-Dha.

238 For the Indian sites, the raw EC measurements of the turbulent wind vectors (u , v and w , for
239 horizontal, meridional and vertical, respectively), sonic temperature (T), and CO_2 and water vapor
240 mass density were recorded at a sampling rate of 20 Hz. Raw EC data were post-processed to
241 obtain level-3 quality controlled and harmonized surface fluxes at 30-minute flux averaging
242 intervals using EddyPRO® Flux Calculation Software (LI-COR Biosciences, Lincoln, Nebraska,
243 USA) using the data handling protocol described by Bhat et al. (2019). The EC data from the
244 OzFlux sites was averaged over 30 minutes recorded by the logger and processed through levels
245 using the PyFluxPro standard software processing scripts as mentioned in Isaac et al. (2017). The
246 Level 3 (L3) used in this paper was produced using PyFluxPro (Isaac et al., 2017) employing the
247 Dynamic INtegrated Gap filling and partitioning for Ozflux (DINGO) system as described in
248 Donohue et al. (2014) and Beringer et al. (2016). The quality checked EC data at 30 minute
249 intervals for two AMERIFLUX sites US-Ton and US-Var was acquired from
250 <https://doi.org/10.17190/AMF/1245971> & <https://doi.org/10.17190/AMF/1245984>, respectively.

251 **2.2.2 Remote sensing data**

252 Optical and thermal remote sensing observations available from Moderate Resolution Imaging
 253 Spectroradiometer (MODIS) (Didan et al., 2015) on-board Aqua platform were used in the present
 254 study (Table 2) for estimating G and associated SEB fluxes. These include eight-day land surface
 255 temperature (LST or T_S) at 1:30 pm and 1:30 am, and surface emissivity (ϵ_s) (MYD11A2), daily
 256 surface albedo (α_R) (MCD43A3), 16-day NDVI (MYD13A2). The overpass times of MODIS
 257 Aqua are at 1:30 pm and 1:30 am. The 8-day average values of clear-sky T_S available from
 258 MYD11A2 data were used (Source: <https://vip.arizona.edu/documents/viplab/MYD11A2.pdf>) for
 259 all nine flux tower sites. Since MYD21A2 LST product is known to provide better accuracy (1 –
 260 1.5 K) (Hulley et al, 2016) as compared to MYD11A2 LST over semi-arid and arid ecosystems,
 261 the former was also used in STIC-TI to compare LE and H estimates (see Table 5 in section 4.4)
 262 with the estimates of MYD11A2 LST over the arid and semi-arid sites (IND-Jai, IND-Naw, US-
 263 Ton). The noon-night pair of thermal remote sensing observations from Aqua are close to the time
 264 of occurrences of maximum and minimum soil surface temperature (see Figure 2) and are therefore
 265 ideal for soil heat flux modeling using thermal inertia. The MODIS Terra overpass times are at 11
 266 am and 11 pm and are far from the time of occurrences of minimum-maximum soil temperatures.
 267 Therefore, MODIS Aqua acquisition times were used in the present study.

268 **Table 2:** A summary of MODIS Aqua optical and thermal remote sensing products used in the
 269 present study

Data type	Product ID (version)	Variables used	Spatial resolution (m)	Temporal resolution	Purpose	Inputs to equation numbers
LST and emissivity	MYD11A2 (V006) MYD21A2	T_S (1:30 pm and am) and ϵ_s	923	8-day	For estimating R_{Ni} , G_i , LE_i , H_i	(5), (13), (C6), (C7), (B8)
Surface albedo	MCD43A3 (V006)	α_R	462	8-day composite from daily	For estimating R_{Ni} , G_i	(5), (B3)

Vegetation index	MYD13Q1 (V006)	NDVI	250	16-day	For estimating G_i	(4)
------------------	----------------	------	-----	--------	----------------------	-----

270 **3 Methodology**

271 **3.1 Coupled soil heat flux-SEB model**

272 In this paper, we modified a thermal inertia (TI) based soil heat flux (G) model using noon-night
 273 thermal remote sensing observations and thereafter coupled the TI-based G with STIC1.2. A clear-
 274 sky net radiation (R_N) model was also introduced into this coupled model and R_N estimation
 275 algorithm is described in Appendix B. The estimation of G through modifying MV2007-TI
 276 approach and its coupling with STIC1.2 is the most novel component of the modeling scheme, and
 277 it is therefore described in the main body of the paper (section 3.1.1). Such a coupling enabled the
 278 implementation of a mechanistic G model along with an analytical SEB model using optical-
 279 thermal remote sensing data. The coupled model is hereafter referred as STIC-TI.

280 **3.1.1 MV2007 soil heat flux model based on Thermal Inertia (TI)**

281 The functional form for estimating instantaneous G (G_i , hereafter) (eq. 2 below) is based on the
 282 harmonic analysis of soil surface temperature and is described in detail by Murray and Verhoef
 283 (2007) and Maltese et al. (2013).

$$G_i = \Gamma \left[(1 - 0.5f_C) \left(\sum_{n=1}^k A \sqrt{n} \omega \sin \left(n\omega t + \phi'_n + \frac{\pi}{4} - \frac{\pi \Delta t}{12} \right) \right) \right] = \Gamma J_s \quad (2)$$

284 G_i is the soil heat flux at the surface at a particular instance (Wm^{-2}), Γ is the soil thermal inertia (J
 285 $m^{-2} K^{-1} s^{-0.5}$), k is the total number of harmonics used, A is the amplitude ($^{\circ}C$) of the n^{th} soil
 286 surface temperature (T_{ST}) harmonic, ω is the angular frequency ($rad s^{-1}$), t is the time (s), ϕ'_n is the
 287 phase shift of the n^{th} soil surface temperature harmonic (rad), J_s is the summation of harmonic
 288 terms of soil surface temperature (K), and Δt (s) is time offset between the canopy composite
 289 temperature and the below-canopy soil surface temperature. Here, we represent G_i and A as
 290 ecosystem-scale ($\leq 1km$) soil heat flux and surface soil temperature amplitude (averaged from soil
 291 surface to 10 cm depth), respectively and assume it to be valid for different vegetated landscape.

292 Since we have considered a single pair (noon-night corresponding to 1:30 pm and 1:30 am) of
 293 MODIS aqua LST data in the present study, the phase shift (ϕ'_n) is taken as zero and number of
 294 harmonics is taken as one ($k=1$) for estimating G_i . Thus equation (2) is modified as follows:

$$G_i = \Gamma \left[(1 - 0.5f_c) \left(A\sqrt{\omega} \sin \left(\omega t' + \frac{\pi}{4} - \frac{\pi \Delta t}{12} \right) \right) \right] = \Gamma J_s \quad (3)$$

295 ~~Δt is found to be 1.5 h (Murray and Verhoef, 2007).~~ With the two boundary values (i.e., $\Delta t=1.5$
 296 h for $f_c = 1$ and $\Delta t = 0$ for $f_c = 0$, f_c being the vegetation fraction), a linear approach is proposed
 297 here to describe the time offset Δt as a function of ~~vegetation fraction (f_c)~~ (Maltese et al., 2013).
 298 For a given day, f_c was derived by normalizing from NDVI on a given day or period and from with
 299 the upper-lower limits of annual NDVI cycle.

$$\Delta t = 1.5 f_c \quad (4)$$

300 **3.1.1.1 Scaling function for estimating ecosystem-scale surface soil temperature amplitude (A)**

301 Estimating ecosystem-scale A involves two steps, (a) computing point-scale soil surface
 302 temperature amplitude (from surface to 0.1m depth) (T_{STA} , hereafter) from the available
 303 measurements of soil surface temperature, and (b) linking T_{STA} with remote sensing variables to
 304 develop scaling functions for A. Point-scale soil temperature measured at different depths within
 305 top 10 cm soil layer at AU-ASM, US-Ton, US-Var was averaged and considered as representative
 306 surface soil temperature (0 – 10 cm). For Ind-Dha and AU-Ade, single-depth (10 cm) soil
 307 temperature measurement was used. Studies also showed that LST carries some signal beneath the
 308 skin of the surface (Johnston et al., 2022).

309 Several studies suggested theoretical sinusoidal trajectory of soil surface and sub-surface
 310 temperatures (Gao et al., 2010), where the amplitude is maximum at the surface, and it gradually
 311 decreases with depth to become 37% of surface amplitude until the damping depth (Hillel, 1982).
 312 However, at deeper depths, soil temperatures remain constant with time and do not show many
 313 fluctuations as compared to surface or near-surface soil temperatures. This invariant soil
 314 temperature is called deep soil temperature (Mihailovic et al., 1999). However, the diurnal surface
 315 soil temperature measurements (within top 0.1 m depth) across different flux tower sites showed
 316 a sinusoidal-exponential behavior, i.e., sinusoidal pattern from sunrise until the afternoon and

317 exponential pattern from afternoon through sunset to the next sunrise. An illustrative example of
 318 the theoretical and observed trajectories of surface soil temperature is shown in Fig. 2. This diurnal
 319 surface soil temperature variation has a single harmonic component (Gao et al., 2010). For
 320 computing T_{STA} , theoretical half-curve of sinusoidal pattern is assumed and was derived from
 321 measurements as exemplified in Fig 2.

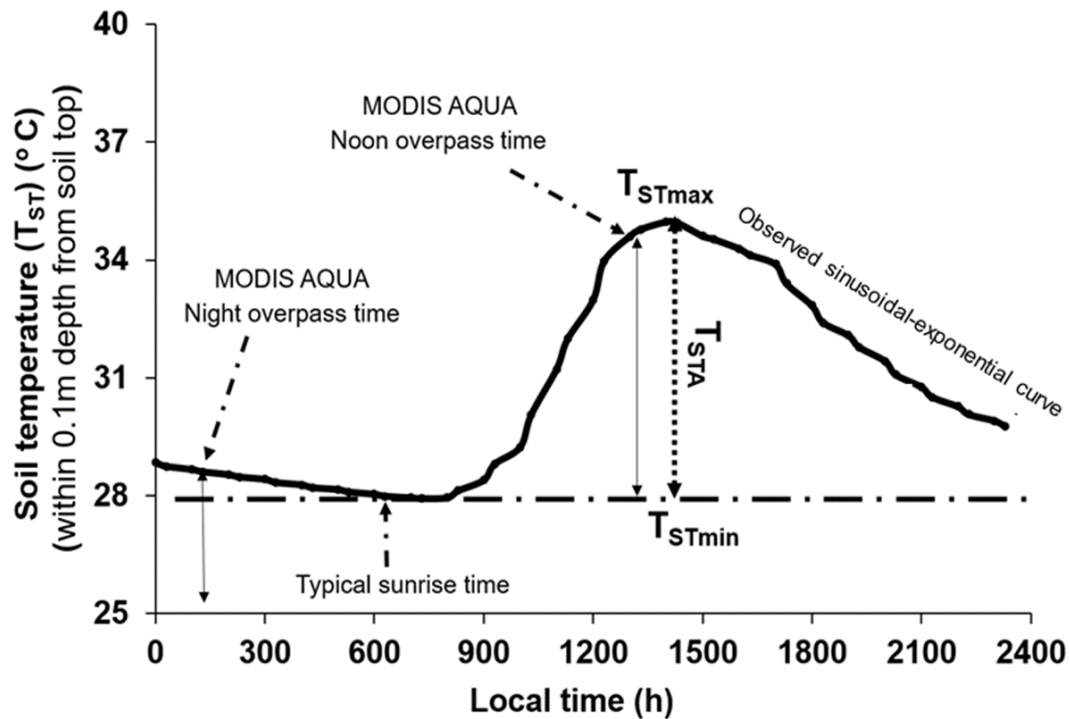


Figure 2. An illustrative example of typical diurnal variation of observed soil temperature (T_{ST}) (from surface to 0.1m depth) at OzFlux sites and timings of MODIS AQUA observations. Here, T_{STmax} and T_{STmin} are maximum and minimum point-scale observed soil surface temperatures

322
 323 It is evident from Fig. 2 that T_{STmin} represents minimum surface soil temperature occurring 1-1.5h
 324 after sunrise and T_{STmax} occurs during 12.30 – 15.00h local time. The *in-situ* measured T_{ST} on
 325 completely clear-sky days at OzFlux sites were used to extract T_{STmax} and T_{STmin} and T_{STA} was
 326 derived as $(T_{STmax} - T_{STmin})$ from the theoretical half-curve of sinusoidal pattern.

327 T_{STA} is generally influenced by several land surface characteristics such as surface temperature
 328 and surface albedo of soil-canopy complex, surface heat capacities, fractional canopy cover and
 329 thermal conductivity (White, 2013). T_S and α_R are the major thermal and reflective land surface
 330 properties that have strong synergy with surface soil temperature dynamics. Hence, we have used
 331 bivariate regression analysis to develop a scaling function for estimating ecosystem-scale T_{STA} (top

332 to 0.1m depth). The bivariate regression is based on the difference of noon (d) and night (n) T_s
 333 data and α_R (Duan et al., 2013, Li Tian et al., 2014) from MODIS Aqua. The scaling function given
 334 in eq. (5) estimates ecosystem-scale T_{STA} (symbolized as ‘A’ in equation 5) from surface to 0.1 m
 335 soil depth:

$$A = B_1(T_{Sd} - T_{Sn}) + B_2(\alpha_R) + B_3 \quad (5)$$

336 Here, B₁, B₂, B₃ are coefficients of regression model; T_{Sd} and T_{Sn} are noon and nighttime LST,
 337 respectively. The results of this regression analysis are elaborated in section 4.1.

338 *3.1.1.2 Estimating Γ*

339 Γ is the key variable for estimating G_i using eq. (2). MV2007 adopted the concept of normalized
 340 thermal conductivity (Johansen, 1975) and developed a physical method to estimate Γ as follows:

$$\Gamma = e^{[Y'(1 - S_r^{(\gamma' - \delta)})]}(\tau_* - \tau_0) + \tau_0 \quad (6)$$

341 where τ_* and τ_0 are the thermal inertia for saturated and air-dry soil ($J m^{-2}K^{-1}s^{-0.5}$); $\tau_0 = D_1\theta^* + D_2$;
 342 $\tau_* = D_3(\theta^{*-1.29})$; $Y'(-)$ is a parameter depending on the soil texture (Murray and Verhoef, 2007;
 343 Minasny, 2007; Anderson et al., 2007); $S_r (m^3 m^{-3})$ is relative saturation and is equal to (θ/θ^*) ; δ
 344 (unitless) is the shape parameter which is dependent on the soil texture. $\theta^* (m^3 m^{-3})$ is the soil
 345 porosity (equal to the saturated soil moisture content when soil moisture suction is zero), $\theta (cm^3$
 346 $cm^{-3})$ is the volumetric soil moisture and D_1, D_2, D_3 are coefficients which were derived from a
 347 large number of experimental data. The reported global values of $D_1, D_2,$ and D_3 were taken as -
 348 1062.4, 1010.8, 788.2, respectively (Maltese et al., 2013). The value for θ^* and shape parameter
 349 for soil textures across study sites were specified according to Van Genuchten et al. (1980). The
 350 details are mentioned in Table E1 of Appendix E.

351 In the present study, the relative soil moisture saturation, $S_r (\theta/\theta^*)$ is represented in terms of an
 352 aggregated moisture availability (M) of canopy-soil complex through a linear function (eq. 12). In
 353 case of zero canopy cover, M represents the soil moisture availability from surface to 0.1 m depth.
 354 In sparse and open canopy, rates of moisture availability from soil to root and root to canopy were
 355 assumed same.

356 Theoretically, M is expressed as available soil moisture fraction between field capacity (θ_{fc}) and
 357 permanent wilting (θ_{wp}) point as given in eq. (7) below.

$$M = \frac{\theta - \theta_{wp}}{\theta_{fc} - \theta_{wp}} \quad (7)$$

358 Where, θ_{fc} ($m^3 m^{-3}$) is the volumetric soil moisture at the field capacity (at a suction of 330 hPa)
 359 and θ_{wp} ($m^3 m^{-3}$) is the volumetric soil moisture at the permanent wilting point (at suction of 15000
 360 hPa) (Singh, 2007). Since θ_{fc} , θ_* , θ_{wp} are characteristic volumetric soil moisture contents
 361 corresponding to specific suctions and depends on the soil texture, dividing the numerator and
 362 denominator in eq. (7) by θ_* gives the following expression:

$$M = \frac{\frac{\theta}{\theta_*} - \frac{\theta_{wp}}{\theta_*}}{\frac{\theta_{fc}}{\theta_*} - \frac{\theta_{wp}}{\theta_*}} \quad (8)$$

363 Due to their dependence on soil texture, the ratios (θ_{fc}/θ_*) and (θ_{wp}/θ_*) are treated as constants.
 364 These are represented as C and C' in the later equations (eq. 9, 10, and 11). The constants, C and
 365 C' vary from 0.3 to 0.8 and from 0.1 to 0.4 (Murray and Verhoef, 2007; Minasny et al., 2011;
 366 Anderson et al., 2007), respectively over different soil textures.

$$M = \frac{\frac{\theta}{\theta_*} - C'}{C - C'} \quad (9)$$

$$M(C - C') = \left(\frac{\theta}{\theta_*}\right) - C' \quad (10)$$

367 By replacing S_r in eq. (6) as θ/θ_* and by rearranging eq. (10), the following linear function is
 368 obtained.

$$S_r = \frac{\theta}{\theta_*} = M(C - C') + C' = M' \quad (11)$$

369 Thus, the modified equation to calculate Γ is given by eq. (12) as follows:

$$\Gamma = e^{\left[\gamma' \left(1 - M'(\gamma' - \delta) \right) \right]} (\tau_* - \tau_0) + \tau_0 \quad (12)$$

370 By substituting the values obtained from eq. (4), (5) and (12) into eq. (3), we obtained the
 371 instantaneous ecosystem-scale G_i corresponding to MODIS Aqua noontime overpass. The intrinsic
 372 link between G_i estimates through MV2007-TI and SEB scheme in STIC1.2 is made through M ,
 373 where the computation of M follows the procedure as described in Mallick et al. (2016, 2018a, b)
 374 and Bhattarai et al. (2018). (description in Appendix C).

375 **3.1.1.3 Estimating M**

376 In STIC1.2, an aggregated moisture availability (M) of canopy-soil complex is expressed as the
 377 ratio of the ‘vapor pressure difference’ between the aerodynamic roughness height of the canopy
 378 (i.e., source/sink height) and air to the ‘vapor pressure deficit’ between aerodynamic roughness
 379 height to the atmosphere:

$$M = \frac{(e_0 - e_A)}{(e_0^* - e_A)} = \frac{(e_0 - e_A)}{\kappa(e_S^* - e_A)} = \frac{s_1(T_{0D} - T_D)}{\kappa s_2(T_S - T_D)} \quad (13)$$

380 Where e_0 and e_0^* are the actual and saturation vapor pressure at the source/sink height; e_A is the
 381 atmospheric vapor pressure; e_S^* is the saturation vapor pressure at the surface; T_{0D} is dew point
 382 temperature at the source/sink height; T_S is the LST; T_D is the air dew point temperature; s_1 and s_2
 383 are the psychrometric slopes of the saturation vapor pressure and temperature between $(T_{0D} - T_D)$
 384 versus $(e_0 - e_A)$ and $(T_S - T_D)$ versus $(e_S^* - e_A)$ relationship; and κ is the ratio between $(e_0^* - e_A)$
 385 and $(e_S^* - e_A)$. To solve the eq. (13), estimation of T_{0D} is necessary. An initial estimate of T_{0D} [T_{0D}
 386 = $[(e_S^* - e_A) - s_3 T_S + s_1 T_D] / (s_1 - s_3)$] and M were obtained following Venturini et al. (2008) where
 387 s_1 and s_3 were approximated in T_D and T_S , respectively. However, eq. (13) cannot be directly
 388 solved because there are two unknowns in one equation. However, since T_{0D} also depends on LE
 389 (Mallick et al., 2016, 2018a), an iterative updation of T_{0D} (and M) was carried out by expressing
 390 T_{0D} as a function of LE [$T_{0D} = T_D + (\gamma LE / \rho c_p g_A s_1)$] which is described in detail by Mallick et al.
 391 (2016, 2018a) and Bhattarai et al.(2018). In the numerical iteration, s_1 was not updated to avoid
 392 numerical instability and it was expressed as a function of T_D .

393 **3.1.2 STIC-TI: Coupling modified MV2007-TI and STIC 1.2**

394 The initiation of the coupling between MV2007-TI and STIC1.2 was executed through linking G_i
395 estimates from the modified MV2007-TI with M estimates from STIC1.2. Having the initial
396 estimates of M (through eq. 13), an initial estimation of G_i was made from eq. (2) where S_r in eq.
397 11 was replaced with the initial estimates of M' . From the initial estimates of G_i (eq. 2) and R_{Ni}
398 (equations in Appendix B), initial estimates of LE_i and H_i were obtained through the [Penman-](#)
399 [Monteith Energy Balance \(PMEB\)](#) equation. Analytical expressions of the conductances for
400 estimating H and LE through the PMEB equation were obtained by solving the state equations as
401 described in the Appendix. The process was then iterated by updating T_{0D} [$T_{0D} = T_D +$
402 $(\gamma LE / \rho c_p g_{AS1})$] and M in every time step (as mentioned in Mallick et al., 2016, 2018a), and re-
403 estimating G_i (using eq. 3), net available energy ($R_{Ni} - G_i$), conductances, LE_i and H_i , until stable
404 estimates of LE_i were obtained. The conceptual block diagram and algorithm flow of STIC-TI is
405 shown in Fig. 3a and Fig 3b, respectively.

406

407

408

409

410

411

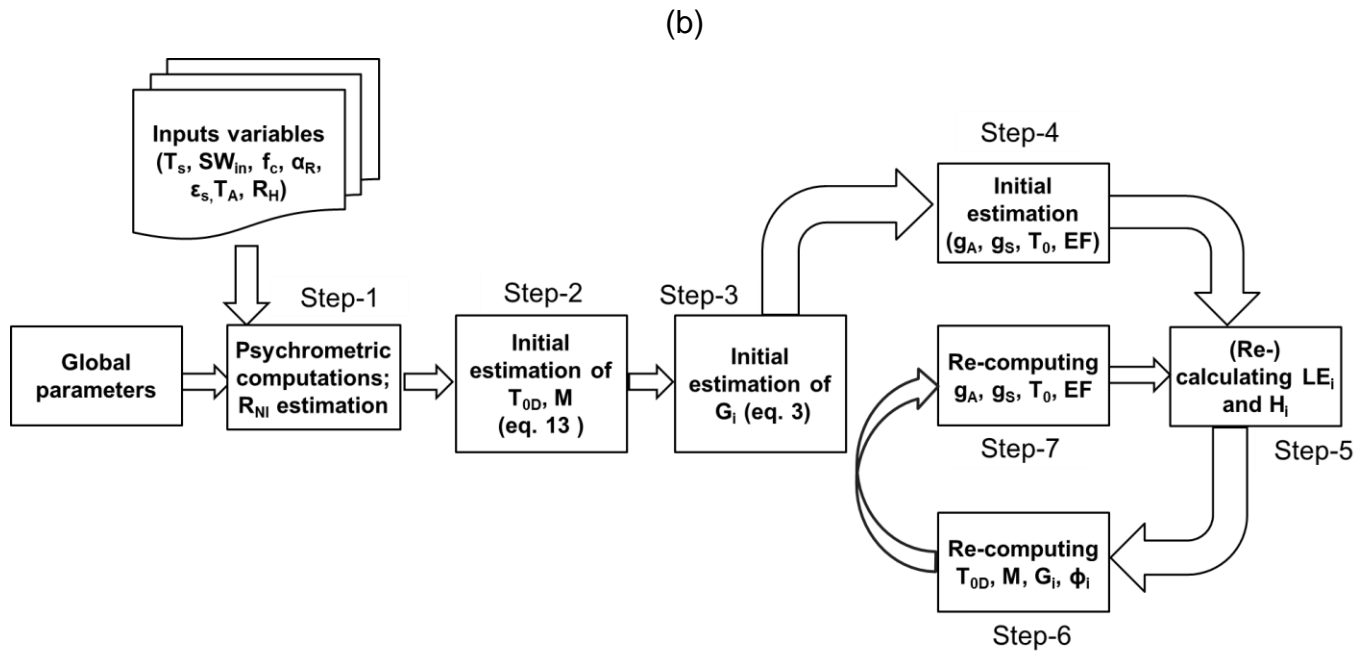
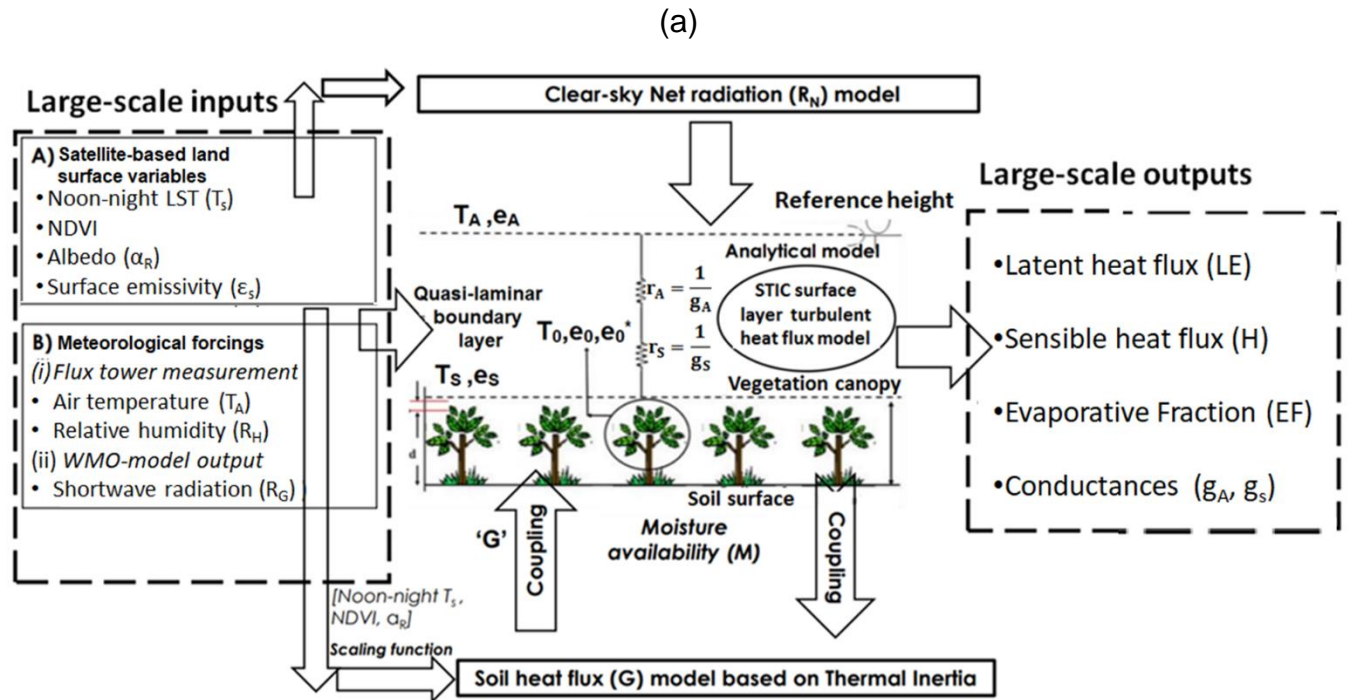


Figure 3: (a) Conceptual diagram of STIC-TI model showing different input variables and model outputs, (b) Algorithmic flow for estimating G and associated SEB fluxes through STIC-TI.

412 Examples of iterative stabilization of G_i and LE_i for Indian, Australian and US ecosystems of India
 413 are shown in Fig. 4. The iterative stabilization of G_i and LE_i was obtained between 8-25 iterations
 414 for all sites.

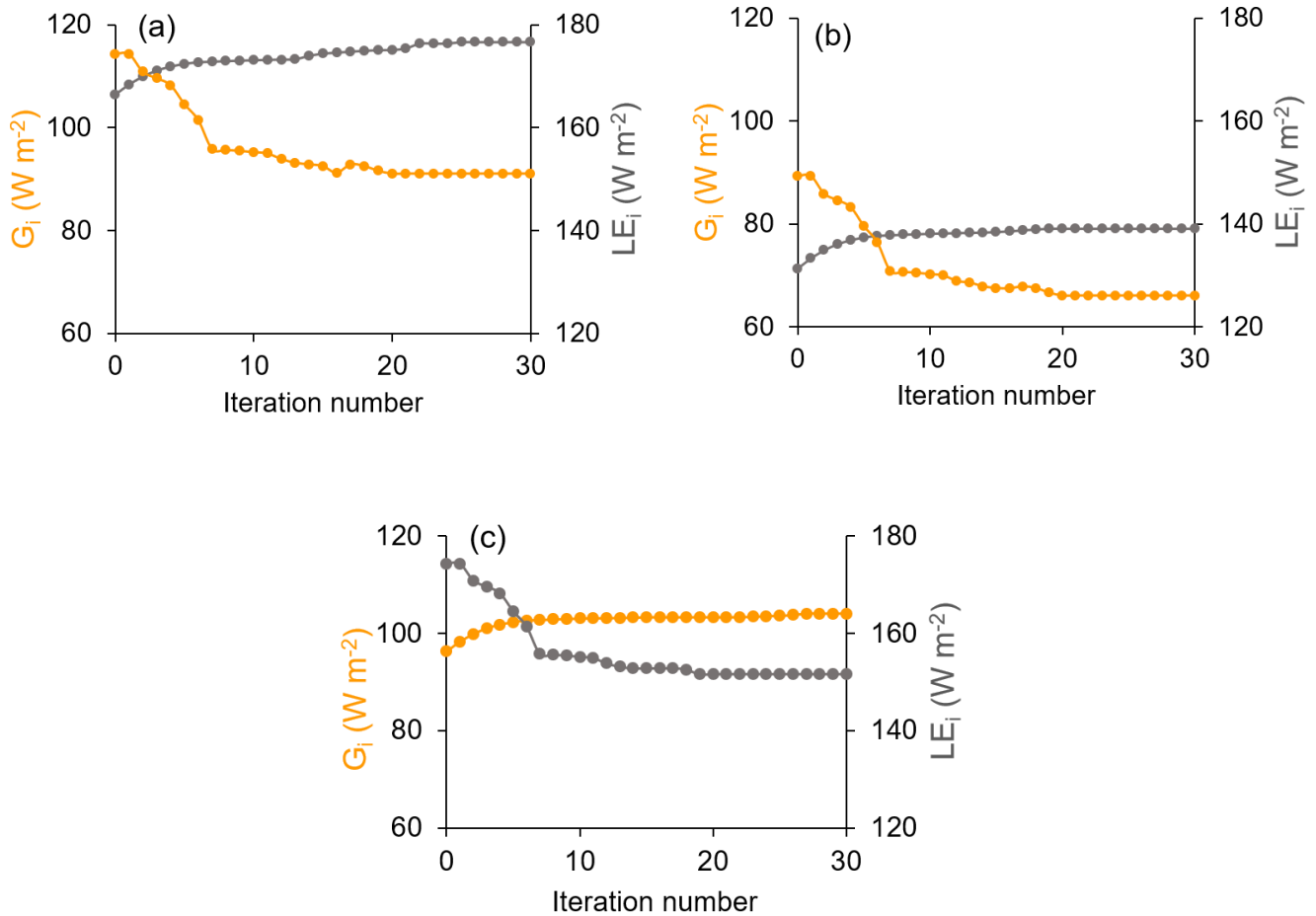


Figure 4: Illustrative examples of iterative stabilization of STIC-TI G_i (yellow marker line) and LE_i (grey marker line) in (a) IND-Jai, (b) AU-ASM, (c) US-Ton

415
 416 The noteworthy features of STIC-TI are: (1) estimating G by modifying the mechanistic MV2007-
 417 TI model using noon and midnight T_s information from thermal remote sensing observations
 418 available through polar orbiting satellite platform (e.g. MODIS Aqua), (2) coupling the
 419 mechanistic MV2007-TI G model with STIC1.2 to simultaneously estimate surface moisture
 420 availability (M), G , and SEB fluxes, (3) introducing water stress information in G (through M) to
 421 better constrain the aerodynamic and canopy-surface conductances as well as the SEB fluxes, and

422 (4) derivation of amplitude of ecosystem-scale surface soil temperature (from top soil to 0.1 m soil
423 depth).

424 **3.1.3 Generation of remote sensing inputs**

425 Two of the key variables in SEB modeling are T_s and ϵ_s . These two variables were retrieved at
426 923m spatial resolution from MODIS Aqua noon-night TIR observations (MYD11A2) in bands
427 11.03 μm and 12.02 μm using a generalized split-window algorithm (Wan et al., 2015). For
428 optimal retrieval, tractable sub-ranges of atmospheric column water vapor and lower boundary air
429 surface temperature were used. Land surface emissivity was estimated from land cover types and
430 anisotropy factors. The MYD21A2 LST product was generated using Temperature-Emissivity
431 Separation (TES) algorithm (Hulley et al, 2016) and improved water vapor scaling method to
432 remove the atmospheric effects. Albedo was estimated from MODIS (MCD43A2 Version 6.0)
433 Bidirectional Reflectance Distribution Function and Albedo (BRDF/Albedo) daily dataset (Schaaf
434 et al., 2002)) at 462 m spatial resolution. Actual albedo is a value which is interpolated between
435 white-sky and black-sky albedo as a function of fractional diffuse skylight (which is a function of
436 aerosol optical depth). NDVI was obtained from level 3 MODIS vegetation indices product
437 (MYD13Q1, version 6.1), which are generated every 16-day at 250 meter (m) spatial resolution.
438 All the input remote sensing variables mentioned in table 2 were resampled to spatial resolution
439 of MYD11A2 product (923 m).

440 **3.2 Sensitivity and statistical analysis**

441 The accuracy of STIC-TI heavily depends on the accuracy of T_s , NDVI, and α_R due to the dual
442 role of T_s in estimating M and G_i , the role of NDVI in G_i , and the combined role of T_s and α_R in
443 estimating R_{Ni} . Therefore, one-dimensional sensitivity analysis was conducted to assess the
444 impacts of uncertainty in T_s , NDVI and α_R on G_i , H_i and LE_i . The sensitivity was assessed by
445 varying noon-time T_s by ± 0.5 K, ± 1.0 K and ± 1.5 K (keeping nighttime T_s constant so that
446 amplitude can vary automatically); varying NDVI by ± 0.05 ; ± 0.10 , ± 0.15 ; and varying albedo by
447 ± 0.02 , ± 0.05 , ± 0.10 , respectively. SEB fluxes were computed by using T_s , NDVI, and α_R for three
448 different periods of the year in all the eight ecosystems. Sensitivity analyses were conducted by
449 increasing and decreasing systematically T_s , NDVI, α_R from its central value while keeping the
450 other variables and parameters constant. This procedure was selected because the fluxes and

451 intermediate outputs of the STIC-TI model reflect an integrated effect due to uncertainty in T_s . In
 452 the first run, SEB fluxes were computed using *in-situ* T_s measurements obtained from the flux
 453 tower outgoing longwave radiation measurements. Then T_s was increased and decreased at
 454 constant interval and a new set of fluxes were estimated. In the similar way, α_R and NDVI were
 455 increased and decreased at constant intervals and new set of fluxes were computed. The sensitivity
 456 of STIC-TI was assessed by the equation 14.

$$\text{Sensitivity} = \frac{E_{i0} - E_{iM}}{O_i} * 100 \quad (14)$$

457 E_{i0} is the estimated (original) model output and E_{iM} is the estimated (modified) output obtained by
 458 changing the variable whose sensitivity is to be tested. O_i is actual measurements. Apart from the
 459 sensitivity analysis, the following set of statistical metrics were used to assess model performances.

$$R^2 = \left(\frac{\sum_{i=1}^n (E_i - \bar{E}) (O_i - \bar{O})}{\sqrt{\sum_{i=1}^n (E_i - \bar{E})^2} \sqrt{\sum_{i=1}^n (O_i - \bar{O})^2}} \right)^2 \quad (15)$$

$$\text{RMSE} = \sqrt{\frac{\sum_{i=1}^n (E_i - O_i)^2}{n}} \quad (16)$$

$$\text{BIAS} = \frac{\sum_{i=1}^n (E_i - O_i)}{n} \quad (17)$$

$$\text{MAPD} = \frac{100}{n} \sum_{i=1}^n \left| \frac{E_i - O_i}{O_i} \right| \quad (18)$$

$$\text{KGE} = 1 - \sqrt{(r - 1)^2 + \left(\frac{\sigma_E}{\sigma_o} - 1 \right)^2 + \left(\frac{\bar{E}}{\bar{O}} - 1 \right)^2} \quad (19)$$

460 Where R^2 is the coefficient of determination, RMSE is root-mean-square error, BIAS is the mean
 461 bias, MAPD is the mean absolute percent deviation, KGE is Kling-Gupta efficiency, n is the total
 462 number of data pairs, the bar indicates mean value of the measured variable and model estimates
 463 of the same variable. E_i and O_i are the model estimated and measured SEB fluxes, r is the Pearson's
 464 correlation coefficient and \bar{O} is the average of measured values and \bar{E} is the average of estimated

465 values and σ_o is standard deviation of observation values and σ_E is the standard deviation of
466 estimated values. The KGE has been widely used for calibration and evaluation hydrological
467 models in recent years and it combines the three components of Nash-Sutcliffe efficiency (NSE)
468 of model errors (i.e., correlation, bias, ratio of variances or coefficients of variation) in a more
469 balanced way. But it has not been widely used for analyzing the ET model performances. $KGE = 1$
470 indicates perfect agreement between modeled estimates and observations. The performance of a
471 model is considered 'poor' for KGE between 0 and 0.5 and models with negative KGE values is
472 considered 'not satisfactory'.

473 **4 Results**

474 **4.1 Ecosystem- scale surface soil temperature amplitude (A)**

475 The scaling functions developed to estimate ecosystem-scale (1km) surface soil temperature
476 amplitude (A) from point-scale T_{STA} were used to estimate G_i . However, before the development
477 of the scaling functions, analysis was carried out to investigate the relationship of soil temperature
478 amplitude between the two different spatial scales. The scatterplot (Fig. 5a) of noon-night LST
479 difference (ΔT_s) versus T_{STA} for different albedo classes showed a linear increase in ΔT_s with
480 increasing T_{STA} . However, some divergence of data points within the cluster were also noticed
481 which could be associated with different albedo (α_R) levels. Bivariate linear function was fitted
482 between T_{STA} as predictand (Y) versus ΔT_s ($T_{sd} - T_{sn}$) and α_R as predictors (X1 and X2,
483 respectively). The function was found to be $Y = 0.59X1 - 51.3X2 + 8.66$ by combining the data
484 of nine ecosystems ($r = 0.86$). The coefficients in the above expressions correspond to B1 (0.59),
485 B2 (51.3), B3 (8.66) of eq. 5 in section 3.1.1.1. The estimated amplitude from this ecosystem-scale
486 predictors and scaling functions was treated as ecosystem-scale surface soil temperature amplitude
487 (A).

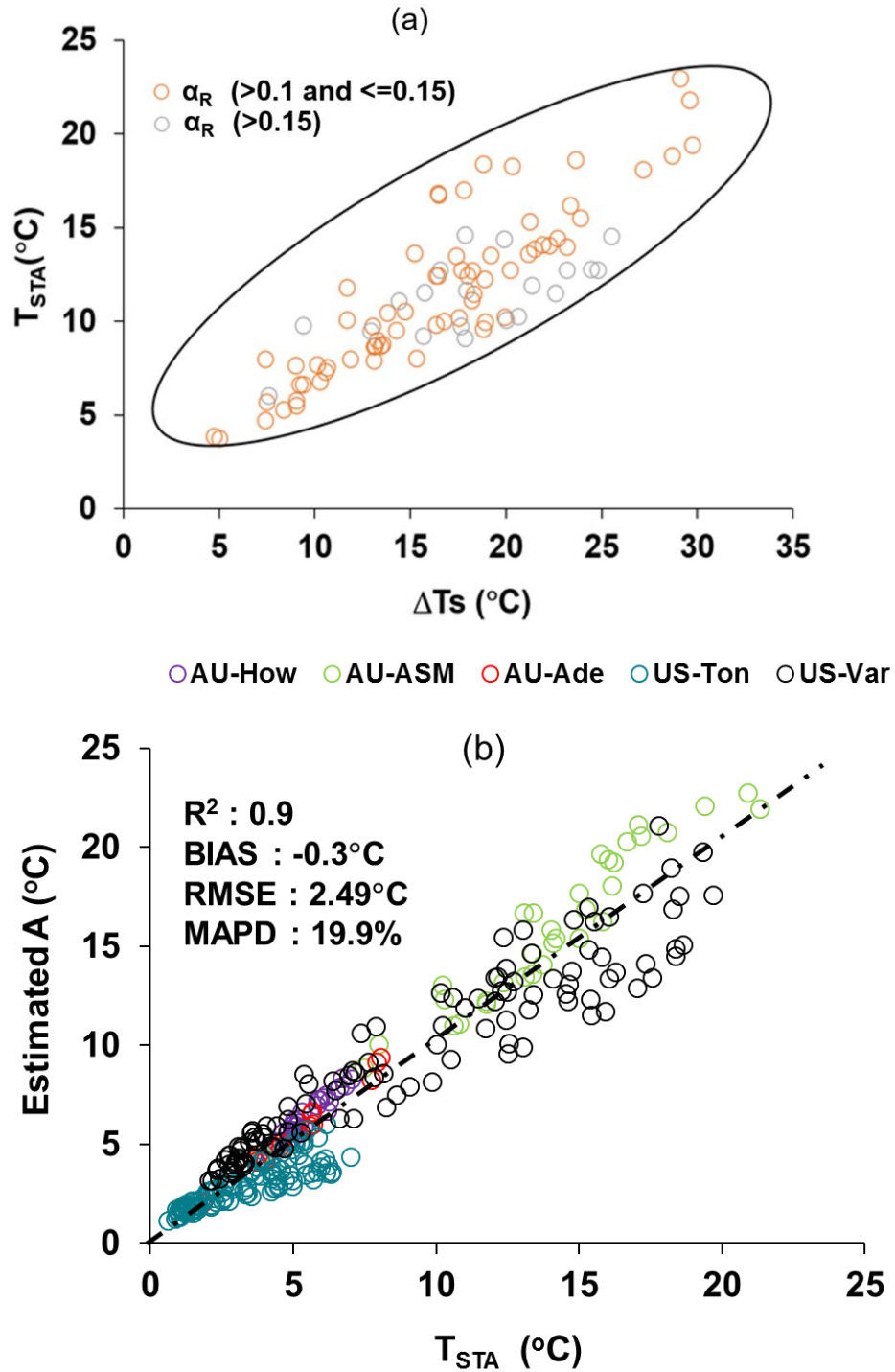


Figure 5. (a) Two-dimensional scatterplots between (ΔT_s) versus T_{STA} at different α_R levels over different ecosystems. Here T_{STA} in y-axis is the observed soil temperature amplitude that is used to develop the scaling function and delta ΔT_s is noon-night LST difference of MODIS AQUA; (b) Validation of ecosystem-scale estimates of A from the above functions over different sites.

488 Validation of ecosystem-scale estimates of A from the above functions over different sites is
489 shown in Fig. 5b with respect to T_{STA} for the independent datasets. The estimated A was found to
490 have MAPD of 19.9%, negative bias, and $R^2 = 0.90$ over different ecosystems. The temporal
491 variation of estimated A and T_{STA} is shown in Fig D1 in Appendix D. Further analysis was carried
492 out to investigate the bias in A at three fractional vegetation cover (f_c) ~~slabs-classes~~ ($f_c < 0.3$; $0.3 \leq f_c \leq 0.5$; $f_c > 0.5$) representing bare soil (~~slab-class~~ 1), 30 – 50% canopy cover (~~slab-class~~ 2) and
493 more than 50% canopy cover (~~slab-class~~ 3), respectively. While negative bias was noted for
494 ~~classslab~~ 1 and ~~classslab~~ 3 (-0.54°C and -0.83°C), the bias was positive (0.49°C) in the
495 intermediate f_c which represents sparse and patchy canopy cover. The signals of surface albedo,
496 emissivity and temperatures of soil surface and canopy are relatively pure in ~~class slab~~ 1 and
497 ~~classslab~~ 3 as compared to ~~classslab~~ 2, where the surface signal carries more heterogeneity. Given
498 T_{STA} is computed from the in-situ measurements, it is likely to carry more heterogeneity in
499 ~~classslab~~ 2 as compared to the other two ~~classesslabs~~. The land surface emissivity in MYD11A2
500 was estimated from land cover types and anisotropy factor, which have differential impacts on T_{ST}
501 and T_s leading to such opposite bias in ~~classslab~~ 2 as compared to ~~classslab~~ 1 and ~~classslab~~ 3.

503 4.2 Sensitivity analysis of STIC-TI G_i , LE_i and H_i to land surface variables

504 4.2.1 Sensitivity of G_i to land surface variables

505 The average sensitivity of G_i to three land surface variables (T_s , NDVI, α_R) by combining the
506 estimates of wet and dry periods is shown in Fig. 6. G_i was found to be substantially sensitive to
507 T_s with error magnitude ranging from 2 – 18% due to T_s uncertainties of $\pm 0.5 - 2.5$ K (Fig. 6a),
508 with greater sensitivity to T_s during the summer season. ~~as compared to other seasons.~~ The median
509 sensitivity of G_i due to $\pm 5 - 10\%$ uncertainty in α_R varied from 5 to 12% in all the ecosystems (Fig.
510 6b). The uncertainties in NDVI revealed 2 to 15% error in G_i estimates (Fig. 6c), and no significant
511 difference in the mean sensitivity due to NDVI uncertainties was noted between the ecosystems.
512 The sensitivity of G_i decreased with increasing values of NDVI.

513 4.2.2 Sensitivity of LE_i and H_i to land surface variables

514 Both LE_i and H_i were sensitive to T_s to the order of 2 – 29% (LE_i) and 5 – 35% (H_i) for T_s
515 uncertainty of $\pm 0.5 - 2.5$ K from its mean values (Table 3). Interestingly, LE_i was more sensitive
516 to T_s uncertainties as compared to H_i in the rainfed ecosystems. The highest mean sensitivity of

517 LE_i to T_S was found in arid (IND-Jai: 2 – 28%), semi-arid (AU-ASM: 5 – 21%), tropical savanna
 518 (IND-Dha: 3 – 26%), savanna (US-Ton: 4-29%) and arid (US-Var: 3-26%) ecosystems. The mean
 519 sensitivity of H_i to T_S was maximum in sub-humid (IND-Sam: 2 – 32%), semi-arid (IND-Naw: 2
 520 – 28%), savanna (AU-Ade: 8 – 17%) (Table 3). A greater sensitivity of the SEB fluxes due to α_R
 521 uncertainties was found than due to NDVI. The median sensitivity of LE_i and H_i due to 10%
 522 uncertainty from mean α_R varied within 2 – 16% in all the ecosystems (Table 3). By contrast,
 523 errors in the two SEB fluxes were substantially low (2 – 13%) due to $\pm 0.05 - 0.15$ uncertainty
 524 from mean NDVI (Table 3).

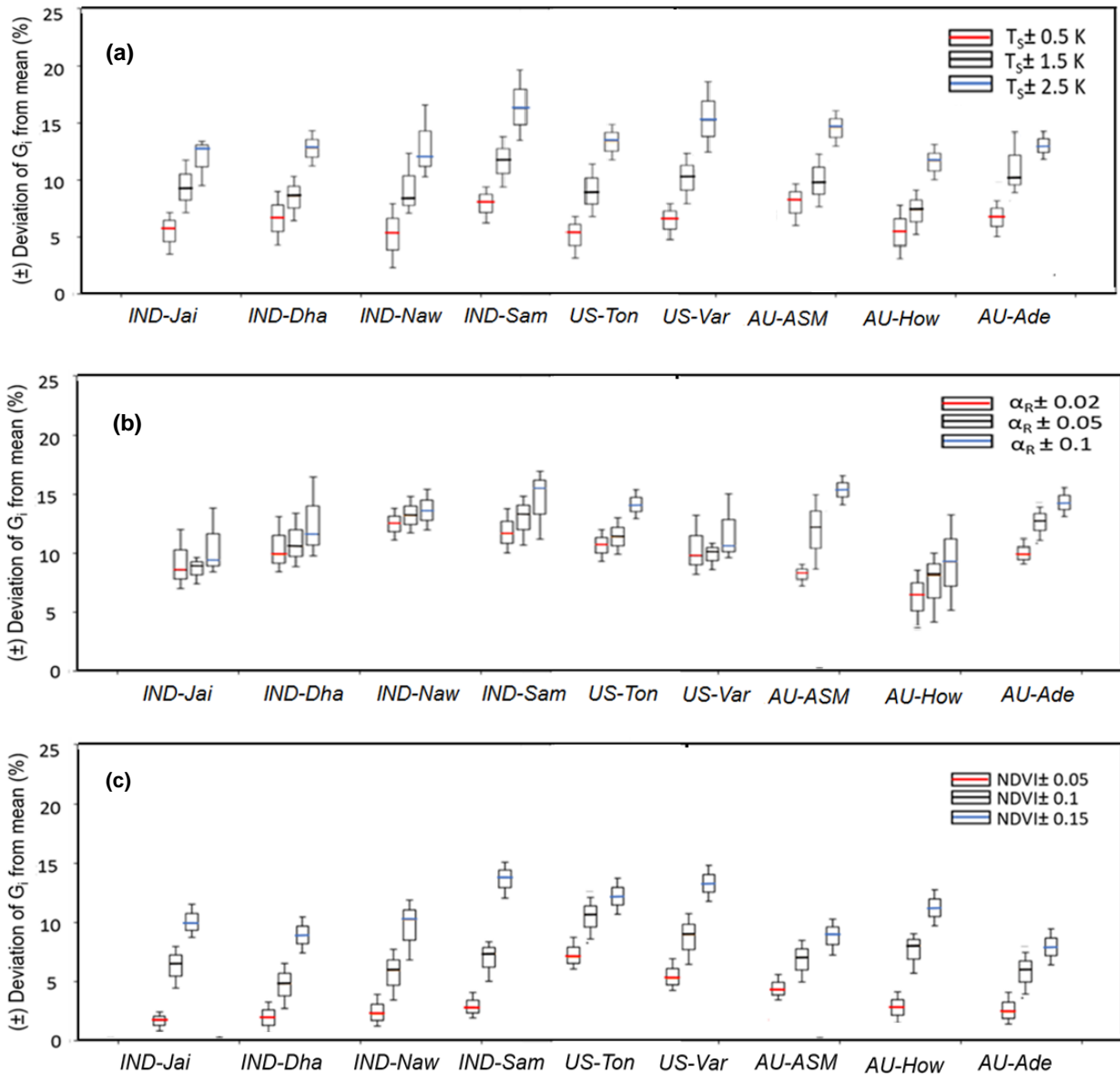


Figure 6: Sensitivity of STIC-TI G_i due to uncertainties in T_s (a), α_R (b), and NDVI (c) for eight flux tower sites in India and Australia. The uncertainties were introduced by taking the mean values of these variables during three different periods (summer, rainy and winter) of a year. Mean uncertainties of the three periods are presented in the figure.

525 **Table 3:** Sensitivity (in percent) of LE_i and H_i due to T_s , NDVI, and α_R uncertainties

Study sites	Sensitivity of LE_i and H_i to T_s , NDVI and α_R (percent change)					
	T_s uncertainty ($\pm 0.5 - 2.5$ K)		α_R uncertainty ($\pm 5 - 10\%$)		NDVI uncertainty ($\pm 0.05 - 0.15$)	
	LE_i	H_i	LE_i	H_i	LE_i	H_i
IND-Jai	2-28	1-6	3-14	2-13	2-8	2-6
IND-Dha	3-26	2-8	2-12	3-12	3-10	3-9
IND-Naw	1-20	2-28	2-10	3-10	2-7	2-6
IND-Sam	1-16	5-32	4-13	6-11	2-5	2-7
US-Ton	4-29	4-12	3-12	4-12	3-8	5-7
US-Var	3-26	6-14	4-11	2-10	4-10	2-8
AU-ASM	5-21	2-10	3-12	2-13	2-10	2-11
AU-How	8-13	2-15	2-11	4-16	3-12	3-13
AU-Ade	2-17	8-17	3-12	2-10	3-10	3-9

526

527 ~~The retrieved G and associated SEB fluxes through STIC-TI were reasonably sensitive to~~
 528 ~~uncertainties in T_s and vegetation index. However, a compensation effect was evident due to the~~
 529 ~~partial cancellation of overestimated TI and underestimated A in the harmonics equation of G .~~
 530 ~~Both, latent and sensible heat fluxes (LE and H), were extremely sensitive to T_s uncertainties, with~~
 531 ~~maximum sensitivity of LE (H) to T_s found in arid and semi-arid (sub-humid) ecosystems.~~

532 **4.3 Comparative evaluation of STIC-TI and contemporary G_i models**

533 The performances of STIC-TI and existing G_i models were evaluated and compared with respect
 534 to *in-situ* G_i measurements. The existing models reported by Moran et al. (1989), Bastiaanssen et
 535 al. (1998), Su (2002), and Boegh et al. (2004) have been considered for comparing with TI-based
 536 model. These four existing models are referred here as MOR89, BAS98, SU02 and BO04,
 537 respectively. While the models MOR89, SU02 and BO04 are based on linear regression between

538 G versus NDVI, BAS98 is based on multivariate regression of G with NDVI, LST and α_R . The
 539 performance of the STIC-TI was substantially better as compared to MOR89, SU02 and BO04
 540 with respect to MAPD (19%), RMSE (22 W m^{-2}) and coefficient of determination ($R^2 = 0.8$) when
 541 compared with *in-situ* measurements over one Indian, three Australian and two US flux tower sites
 542 (Table 4) and also comparable with BAS98 G_i model. The validation plot of retrieved noontime
 543 G_i from STIC-TI is shown in Fig. 7.

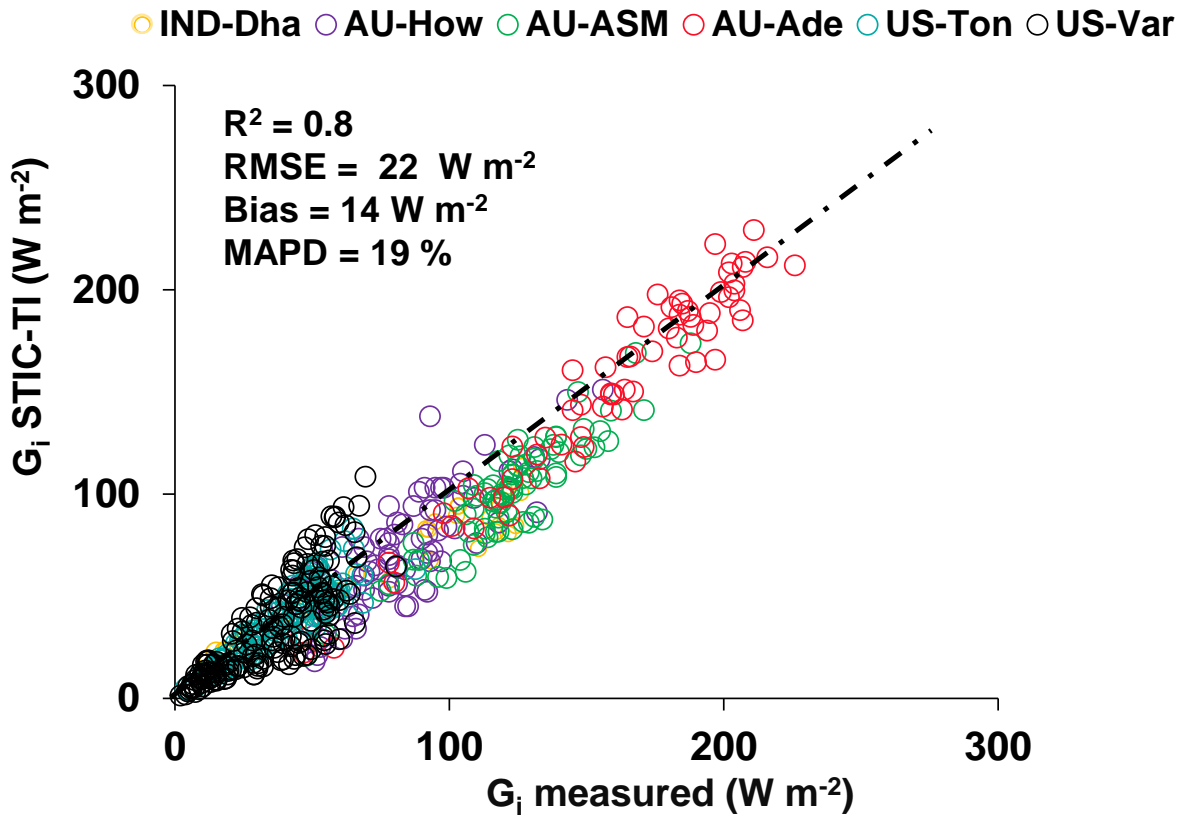


Figure 7: Validation of noontime (1:30 pm) G_i estimates with respect to in-situ measurements in different ecosystems. The regression between the two sources of G_i is $G_i(\text{STIC-TI}) = 0.90G_i(\text{tower}) - 0.10$.

544 **Table 4:** A comparison of error statistics of G_i estimates from STIC-TI and existing G_i models
 545 over different ecosystems

G models	R^2	RMSE (W m^{-2})	MAPD (%)	KGE
STIC-TI	0.80	22	19	0.74
MOR89	0.70	31	29	0.46

BAS98	0.80	20	18	0.61
SU02	0.80	30	26	0.54
BO04	0.70	35	29	0.48

546 The RMSE varied from 9 to 20 $W m^{-2}$ with MAPD ranging from 12 to 21% across individual flux
547 tower sites. High magnitude of G_i was predicted in the arid and semi-arid systems (120 – 240 W
548 m^{-2}) as compared to the humid systems (20 – 90 $W m^{-2}$), which was in close correspondence with
549 the observations. The model also captured the range of G_i that are generally found in different
550 biomes (20 – 140 $W m^{-2}$ for grasslands, 20 – 90 $W m^{-2}$ for cropland) (Purdy et al., 2016). Due to
551 the paucity of G_i measurements, direct validation of G_i was only possible for 32 days (concurrent
552 to MODIS overpass) at the IND-Dha site. Overall, STIC-TI tends to provide reasonable G
553 estimates for the terrestrial ecosystems having soil temperature amplitude above 5°C.

554 4.4 Evaluation of STIC-TI LE_i , H_i , and EF

555 The modeled versus measured LE_i and H_i showed good agreement in all the nine ecosystems with
556 RMSE in LE_i and H_i estimates using MYD11 LST product to the order of 29 – 62 $W m^{-2}$ and 26 –
557 61 $W m^{-2}$, MAPD of 9 – 31% and 20 – 36%, BIAS of -29 to 38 $W m^{-2}$ and -44 to 32 $W m^{-2}$ (Fig.
558 8a, b; Table 5) and high R^2 of 0.8.

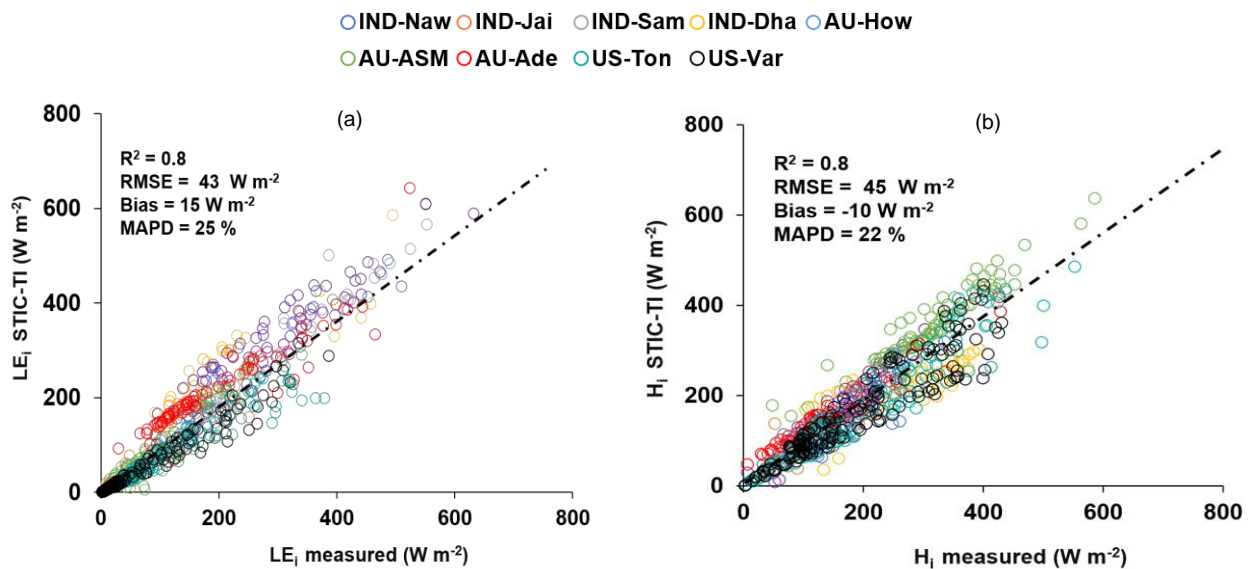


Figure 8: (a) Validation of STIC-TI LE_i estimates with respect to *in-situ* measurements in different ecosystems; (b) Validation of STIC-TI H_i estimates with respect to *in-situ* measurements in different ecosystems.

559

560 **Table 5:** Error statistics of STIC-TI LE_i and H_i estimates with respect to EC measurements in
 561 different ecosystems of India, US, and Australia using MYD11A2 LST product for all nine sites
 562 and using MYD21A2 LST product for three semi-arid and arid sites. The statistics obtained by
 563 using MYD21A2LST are shown in the parentheses.

564

Sites	STIC-TI (LE_i and H_i)									
	R^2		BIAS ($W\ m^{-2}$)		RMSE ($W\ m^{-2}$)		MAPD (%)		KGE	
	LE_i	H_i	LE_i	H_i	LE_i	H_i	LE_i	H_i	LE_i	H_i
IND-Jai	0.90 (0.91)	0.90 (0.92)	-21 (-16)	12 (9)	57 (45)	27 (21)	31 (24)	22 (19)	0.80 (0.82)	0.76 (0.79)
IND-Naw	0.90 (0.92)	0.80 (0.85)	19 (12)	-26 (-16)	44 (37)	51 (46)	17 (16)	28 (25)	0.92 (0.92)	0.71 (0.73)
IND-Dha	0.90	0.90	38	-44	43	35	27	25	0.71	0.64
IND-Sam	0.90	0.80	12	-10	32	61	9	27	0.95	0.70
US-Ton	0.90 (0.91)	0.90 (0.92)	-29 (-18)	-32 (-21)	53 (45)	34 (27)	25 (22)	17 (15)	0.85 (0.87)	0.91 (0.93)
US-Var	0.90	0.80	-19	-28	49	39	27	20	0.82	0.89
AU-ASM	0.90 (0.93)	0.90 (0.91)	-3 (6)	22 (16)	46 (37)	26 (18)	29 (24)	20 (17)	0.94 (0.95)	0.83 (0.85)
AU-How	0.90	0.90	16	-25	42	27	17	21	0.89	0.85
AU-Ade	0.90	0.90	21	15	29	53	28	36	0.77	0.80

565

566 Arid ecosystems in India (IND-Jai), US (Ton and Var) and semi-arid ecosystem in Australia (AU-
 567 ASM) revealed relatively high MAPD (31%, 25%, 27%, and 28%) (Table 5). In general, STIC-TI
 568 was able to produce the dominant convective heat fluxes with respect to the EC measurements as
 569 evident through low RMSE for H_i and high RMSE for LE_i in the IND-Jai, US-Ton, US-Var, and
 570 AU-Ade where LE_i is inherently low except few rainy days. A uniform distribution of data points
 571 around 1:1 validation line (Fig. 8a) indicated overall low BIAS in LE_i estimates. However,
 572 modeled H_i was consistently lower than the observations (negative BIAS) in the tropical savanna
 573 (IND-Dha and AU-How) and semi-arid (IND-Naw) ecosystems [(-44) – (-25) $W\ m^{-2}$ and -26 W
 574 m^{-2}] while a consistent positive BIAS was observed in the AU-ASM (semi-arid) and AU-Ade
 575 (savanna), US-Var (arid) (Fig. 8b; Table 5). This consequently led to overall low negative BIAS
 576 (-10 $W\ m^{-2}$), relatively low R^2 in H_i ($R^2 = 0.8$) as compared to the errors in LE_i (BIAS = 15 $W\ m^{-2}$,
 577 $R^2 = 0.9$). The regression between the modeled and tower measurements of LE_i is $LE_i(\text{STIC-TI})$
 578 $= 0.98LE_i(\text{tower}) - 0.266$. The regression between the modeled and tower measurements of H_i is
 579 $H_i(\text{STIC-TI}) = 0.93H_i(\text{tower}) + 4.90$. The KGE statistics varied in the range of 0.71 – 0.95 for LE_i

580 and in the range of 0.64 – 0.91 for H_i , respectively across all nine flux tower sites, thus revealed
 581 reasonably high efficiency of the model to capture the magnitude and variability of SEB fluxes.

582 The impact of MODIS Aqua day-night view angle difference (δVZA) on STIC-TI fluxes was
 583 further investigated. Estimated errors in terms of mean percent deviation in LE_i , H_i and G_i with
 584 respect to measurements for each 10° bin over 16 angular bins within $\pm 80^\circ$ were analysed in
 585 response to mean δVZA of each angular bin. G_i errors (X) were found to be significantly correlated
 586 with δVZA (Y) in a parabolic ($Y = 0.0027X^2 - 0.0025X + 1.4919$; $r = 0.73$) pattern (Refer
 587 Appendix F, Figure F(a)). Errors in G_i to the order of -5 to 10%, 10-15% and >15% were largely
 588 found to be within $\pm 30^\circ$, $\pm 45^\circ$, and $>45^\circ$ to -80° δVZA , respectively. The errors in H_i were found
 589 to have strong linear ($Y = -0.1452X + 1.1146$, $r = 0.77$) dependence on δVZA (Refer Appendix F,
 590 Figure F(b)). However, a weak dependence of LE_i errors ($Y = -0.0878X + 2.0314$, $r = 0.5$) on
 591 δVZA (Refer Appendix F, Figure F(c)) was found, as majority of the errors were within $\pm 10\%$ that
 592 corresponded to $\pm 60^\circ$ δVZA . The nature of relations and degree of dependency of model flux
 593 errors on δVZA in this study would be helpful to minimize the error budget in surface energy
 594 balance fluxes from future thermal infrared missions having day-night observations.

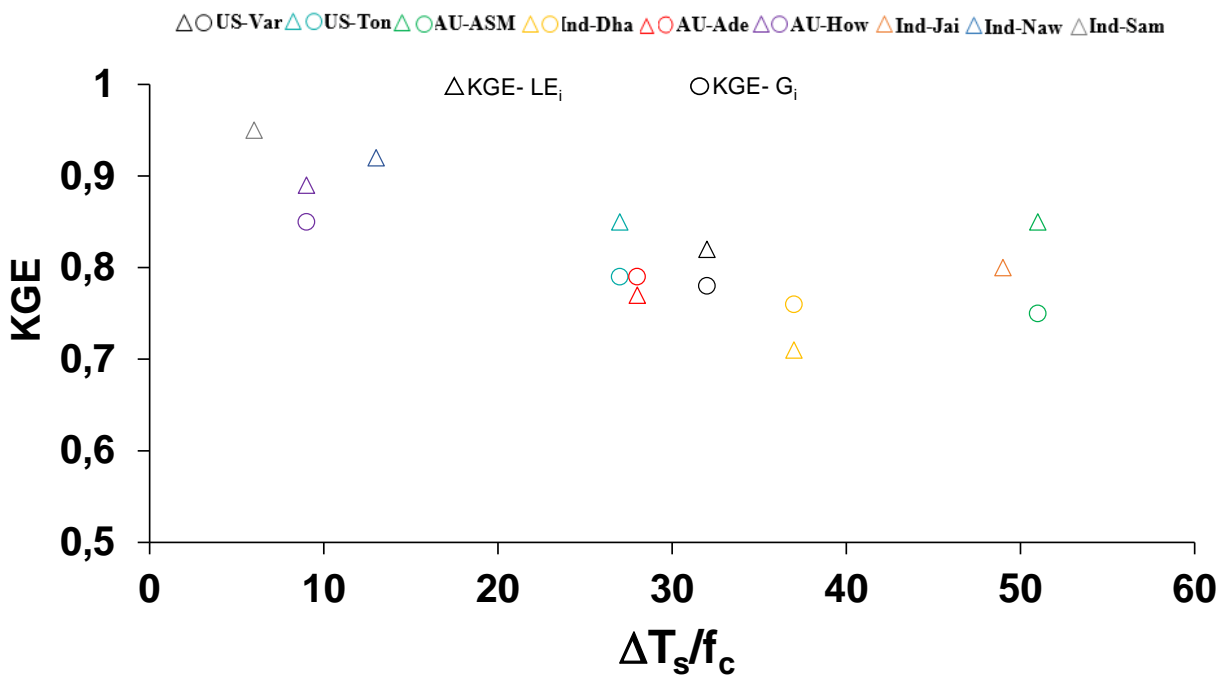


Figure 9: Relationship between KGE of STIC-TI (G_i and LE_i) with $\Delta T_s/f_c$ in different terrestrial ecosystems.

595 Further investigation was made on whether KGE for STIC-TI G_i and LE_i follow any systematic
596 pattern and the ratio ΔT_s and f_c was used as proxy for surface heterogeneity and dryness. The plot
597 of KGE of G_i and LE_i with this ratio is shown in Fig. 9. KGE- G_i was found to show a systematic
598 decrease with increase in ΔT_s - f_c ratio up to 40, after which it remained unchanged with increase
599 in the ratio. Although KGE of LE_i also decreased (20% reduction) with increase in ΔT_s - f_c ratio,
600 KGE- LE_i was found to increase beyond ΔT_s - f_c 40. This revealed that the model efficiency
601 remained high (>0.8) within certain dryness limits (ΔT_s - f_c ratio <20 and >50) and the efficiency
602 reduced moderately (within $0.7 - 0.8$) for intermediate dryness. Interestingly, the use of
603 MYD21A2 LST in STIC-TI showed improvements (see the parentheses in different columns in
604 Table 5) in LE_i and H_i error statistics as compared to using MYD11A2 LST in terms of higher R^2
605 and KGE, and lower RMSE in LE_i (3-8% less) and H_i (2-3% less) for semi-arid and arid sites such
606 as IND-Jai, IND-Naw and US-Ton.

607 An independent evaluation of multi-temporal heat fluxes over two US flux sites for the years 2016-
608 2018 is shown in Fig. 10 and Fig 11. STIC-TI G_i estimates with MYD11A2 LST product showed
609 close match with *in-situ* measurements with respect to intra and inter-annual variability in G_i
610 followed by LE_i and H_i . This further demonstrates the merit of the coupled model for reproducing
611 ecosystem-scale G_i estimates especially for shorter and open canopies.

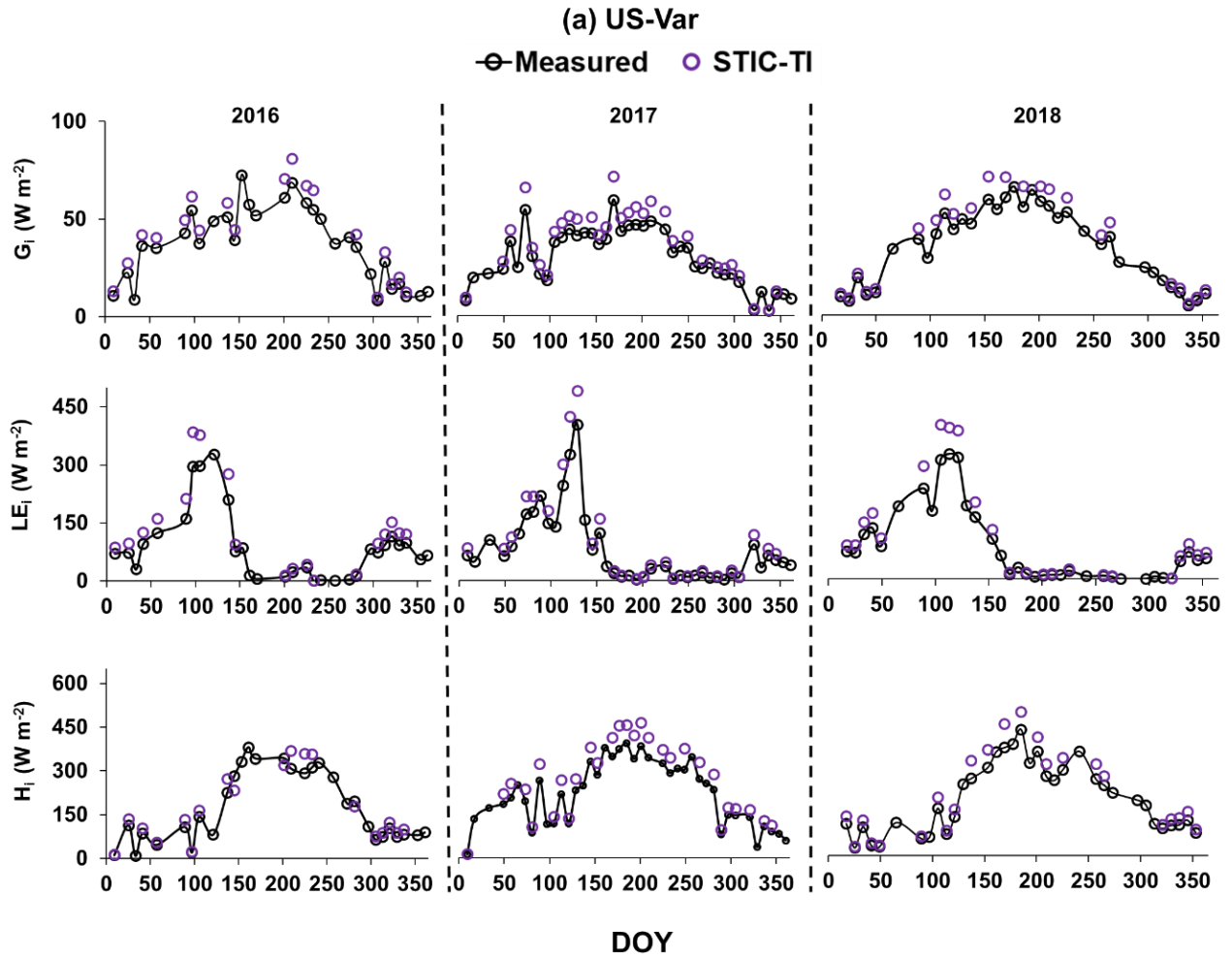


Figure 10: Illustrative examples of temporal evolution of STIC-TI derived fluxes using MYD11A2 LST product versus observed SEB fluxes for three consecutive years from 2016 to 2018 in a grassland ecosystem in United States (e.g., US-Var).

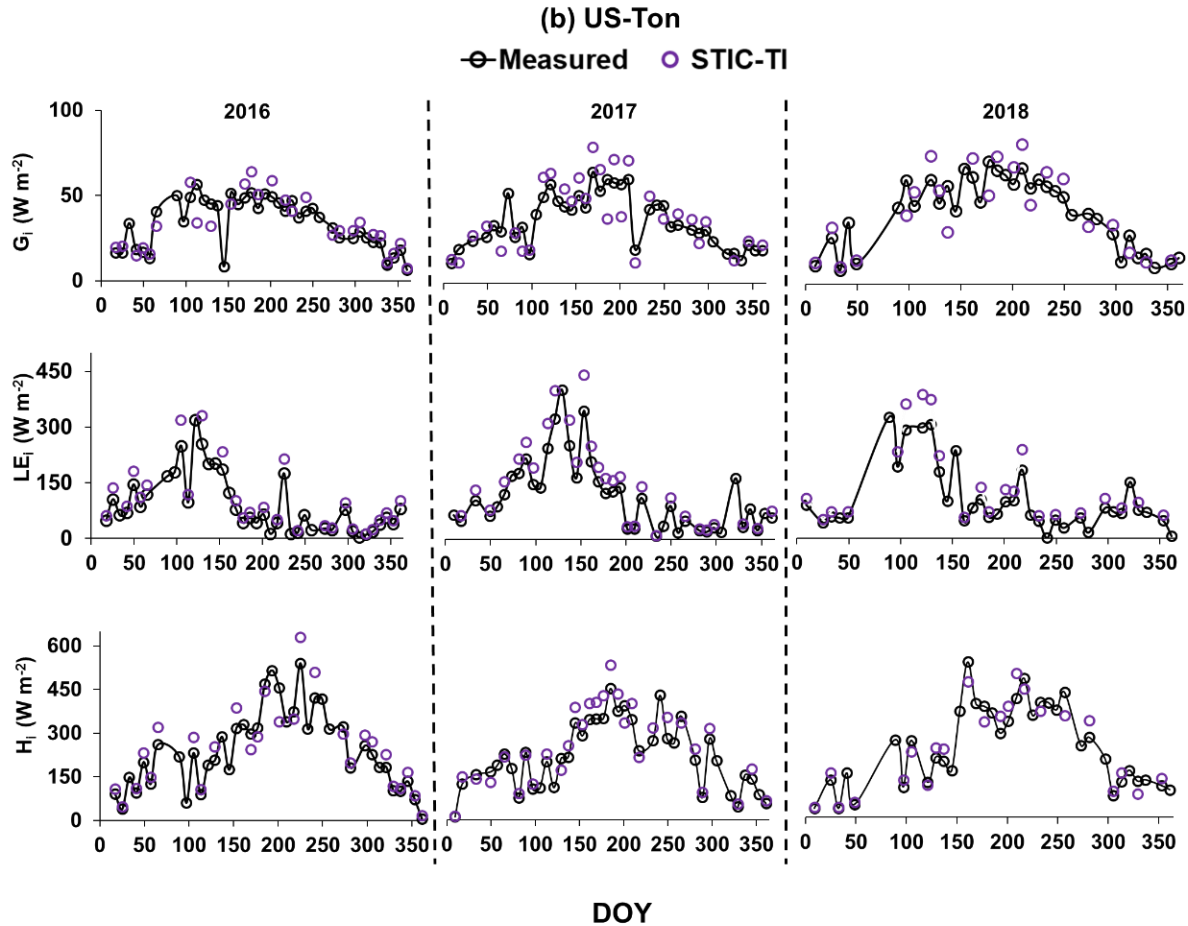


Figure 11: Illustrative examples of temporal evolution of STIC-TI derived fluxes using MYD11A2 LST product versus observed SEB fluxes for three consecutive years from 2016 to 2018 in a woody savanna ecosystem in the United States (e.g., US-Ton).

612 The temporal behavior of STIC-TI and observed evaporative fraction (EF) (ratio of LE and $R_N -$
 613 G) (Fig. 12) along with observed monthly rainfall (P) distinctly captured the substantial temporal
 614 variability in EF during the dry-to-wet transition in the Indian study sites, which also corresponded
 615 to low (high) θ and P. In IND-Naw and IND-Sam, a marked rise (>0.4) in STIC-TI EF was noted
 616 during day-of-the-year (DOY) 25 to 75 where wheat is grown under assured irrigation. The impact
 617 of irrigation is thus captured by the substantial increase in EF in the absence of P. In contrast, the
 618 rainfed grassland system (IND-Jai) showed peak EF (~ 0.8), which corresponded to south-west
 619 monsoon rainfall during June to September and a progressive decline in EF during the dry down
 620 period in October to April corresponding to post south-west monsoon phase. Some intermittent
 621 spikes in EF were also noted during dry-down phase in both STIC-TI and observations. The
 622 intermittent EF spikes during the soil moisture dry down phase could be due to enhanced LE

623 through moisture advection from the surrounding vegetation causing an enhancement of
 624 evaporation than expected. This is known as the ‘clothesline effect’ which frequently occurs in
 625 semi-arid and arid ecosystems. In addition to IND-Jai, the response of both modeled and measured
 626 EF to wet and dry spells was also noted during south-west monsoon period at all other flux tower
 627 sites of India.

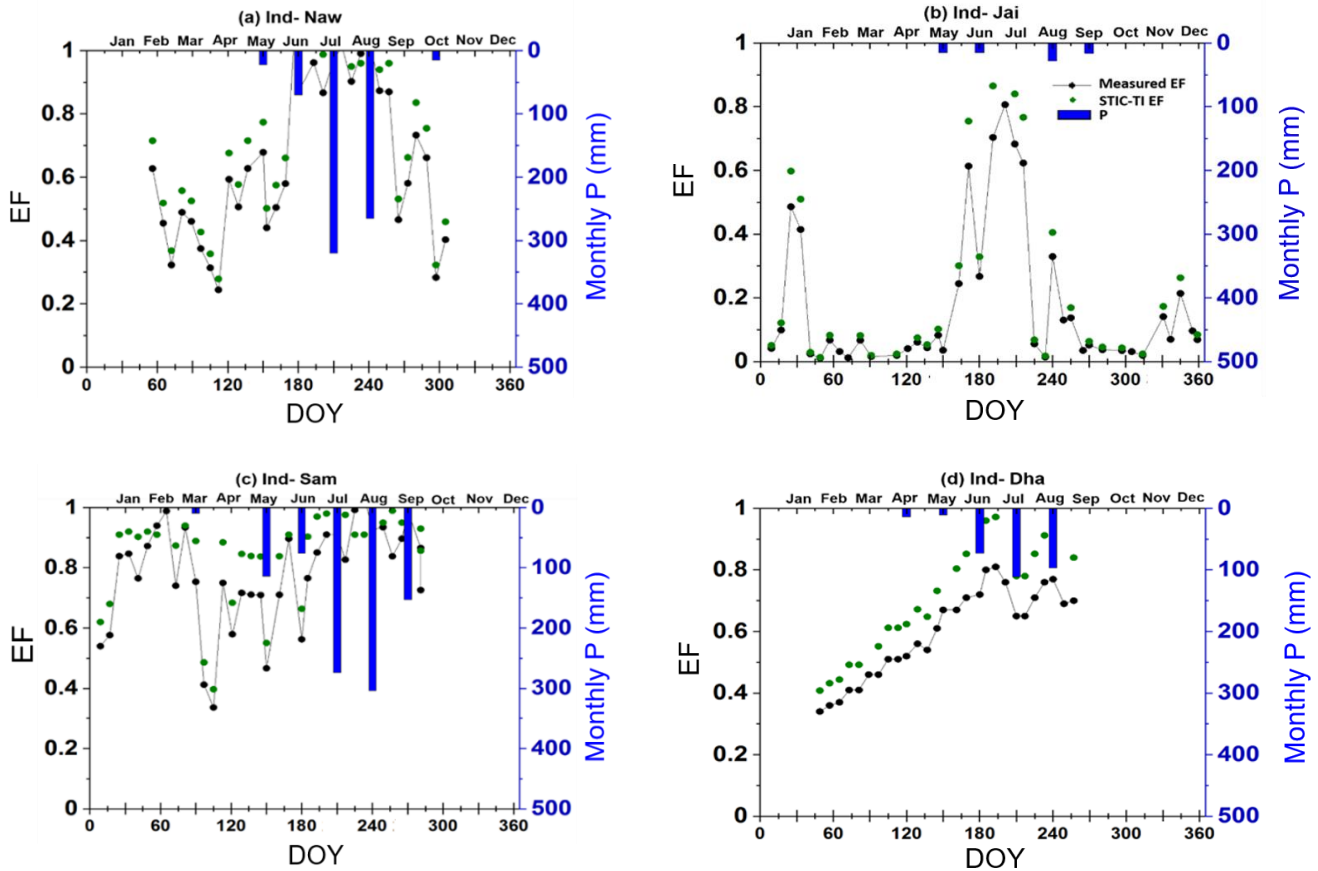


Figure 12: Illustrative examples of temporal variation of STIC-TI derived EF using MYD11A2 LST product with respect to measured EF and P in (a) IND-Naw, (b) IND-Jai, (c) IND-Sam, and (d) IND-Dha

628 The temporal behavior of EF from STIC-TI using MYD11A2 LST product and EC measurements
 629 along with measured θ and P at the OzFlux and AmeriFlux sites also revealed (Fig. 13) close
 630 correspondence of STIC-TI with EC observations. Low EF (0.05 – 0.40) during the dry season
 631 around DOY 100 – 250 and high EF (>0.4) during the wet season (DOY 1 – 120 and 300 to 360)
 632 in AU-ASM, US-Ton and US-Var was observed. The analysis showed that STIC-TI EF can
 633 capture the annual variability of observed EF and its responses across different ecosystems during
 634 wet and dry seasons. The plots of STIC-TI EF versus measured θ (in the inset of Fig. 13) revealed

635 triangular scatter close to right-angled triangle with positive slope of hypotenuse in three
 636 ecosystems AU-ASM, US-Var and US-Ton. This showed that in the water-controlled ecosystems,
 637 where distinct wet-dry seasons exist, the positive EF- θ relationship is an outcome of the soil
 638 moisture controls on transpiration during the dry season.

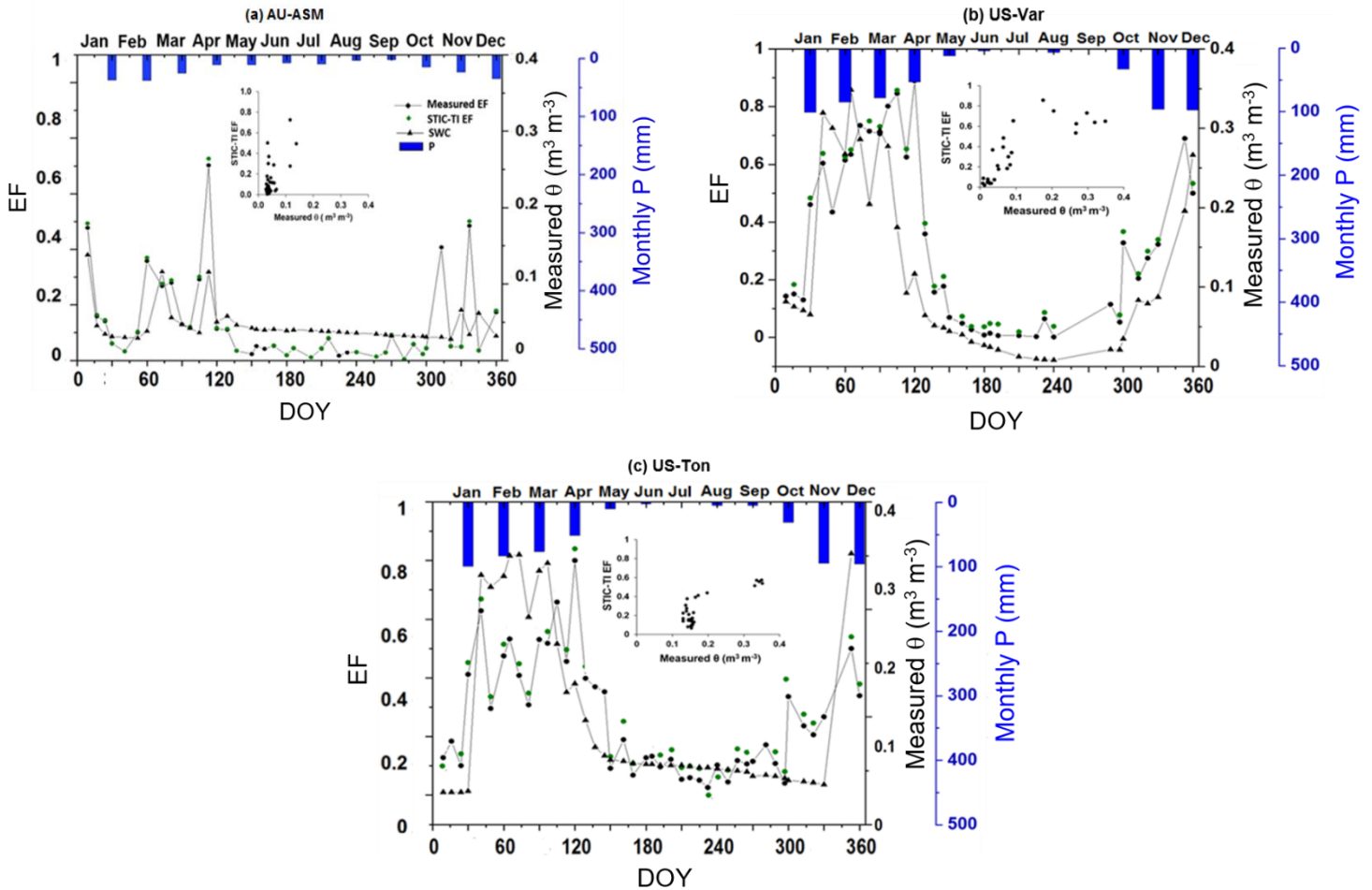


Figure 13: Comparison of temporal variation of STIC-TI derived EF using MYD11A2 LST with respect to measured EF, θ and Pin (a) AU-ASM, (b) US-Var, (c) US-Ton. The scatterplots in the inset shows the relationship between STIC-TI EF with respect to measured θ .

639 5 Discussion

640 5.1 Interaction of flux and internal SEB metrics

641 From section 4.1 we found relatively reduced sensitivity of G_i to T_s uncertainties. In any given
 642 condition, if an over(under) estimation of M due to noontime T_s uncertainties (through eq. 13)
 643 leads to an over(under) estimation of Γ , the effects of such over(under) estimation of Γ (due to

644 noontime T_s uncertainties) tend to be compensated by under(over) estimation of amplitude A (in
 645 eq. 5), ultimately leading to a reduction of the sensitivity of G_i to T_s . While the scatter between G
 646 versus A for a wide range of Γ (Fig. 14a) revealed large scatter with increasing amplitude under
 647 the dry conditions (low Γ), the scatter between Γ versus T_s for different M (Fig. 14b) revealed
 648 exponential reduction of Γ with increasing T_s and dryness, and almost no significant change in Γ
 649 with increasing T_s at a constantly high dryness ($M < 0.25$). Thus, the confounding effects of Γ , A ,
 650 and M through eq. 3, 5, 12 and 13 led to a reduction of sensitivity of G to T_s , as exemplified in
 651 Fig. 14.

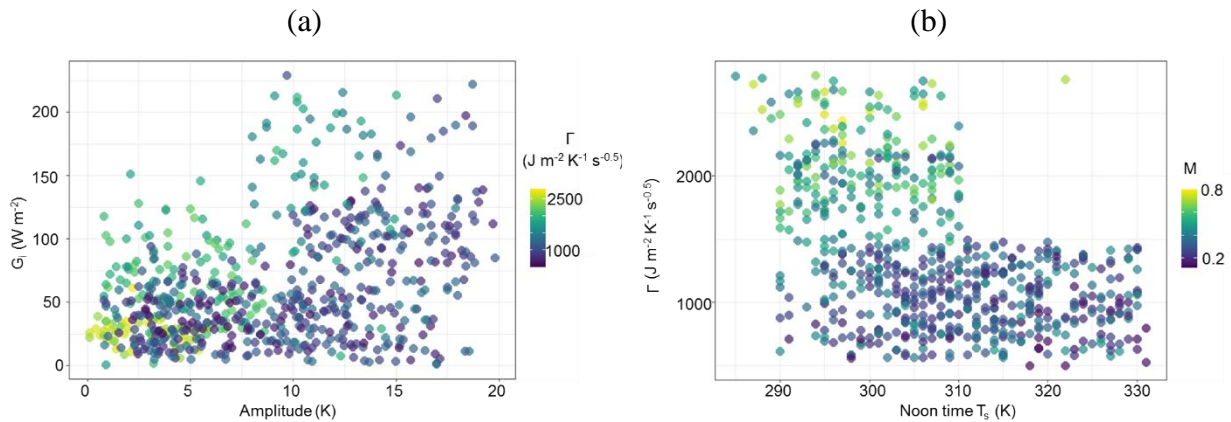


Figure 14: Response plots among parameters of TI-based G_i model, such as (a) G_i versus Amplitude (A) for varying Γ , and (b) Noon-time T_s versus Γ with varying M .

652
 653 Concerning LE_i and H_i , dual uncertainties could be propagated in both the fluxes through
 654 daytime T_s (through M and G_i), leading to high sensitivity of these two SEB fluxes due to T_s
 655 perturbations. The relatively high sensitivity of LE_i to T_s (as compared to H_i) in the non-
 656 irrigated ecosystems could be due to partial compensation of g_A/g_s in both numerator and
 657 denominator of the PMEB equation for H (eq. C7 of Appendix C). A recent study (Fig.10 in
 658 Mallick et al., 2018a) showed high sensitivity of g_s due to T_s (1% change in T_s led to 5.2–7.5%
 659 change in g_s) as compared to g_A sensitivity to T_s (1% change in T_s led to 1.6–2% change in g_A),
 660 suggesting that errors in g_s due to T_s uncertainty tend to be larger than errors in g_A . Partial
 661 cancellation of the conductance errors in the numerator of eq. (C7 of Appendix C) might have
 662 resulted in compensation of H_i errors in the water-limited ecosystems. In this environment, the
 663 variability of LE_i is mainly dominated by g_A/g_s , which makes LE_i highly sensitive due to T_s
 664 uncertainties. Combined uncertainty due to g_A/g_s in the denominator and g_A in the numerator

665 of eq. (C6 of Appendix C) resulted into greater sensitivity in LE_i to T_s in the arid and tropical
666 savannah ecosystems (Mallick et al., 2015, 2018a; Winter & Eltahir, 2010). The very low
667 sensitivity of LE_i and H_i due to uncertainties in NDVI is because NDVI was not used in the
668 conductance parameterizations and effects due to NDVI in STIC-TI was only propagated
669 through G_i . The sensitivity of LE_i and H_i to albedo was mainly due to the dependence of net
670 radiation (R_{Ni}) on albedo, and any resultant uncertainty in R_{Ni} (due to albedo) tends to be
671 reflected in the sensitivity of LE_i and H_i to albedo.

672 **5.2 Possible sources of errors in SEB flux evaluation**

673 In STIC-TI, underestimation and overestimation errors in G_i in different ecosystems (Fig. 7) could
674 originate due to the errors in MYD11A2 LST product. A host of studies previously reported that
675 the standard deviations of errors in retrieved emissivity in bands 31 and 32 are 0.009, and the
676 maximum error in retrieved T_s of MOD11A1 LST falls within 2-3 K, which is mainly due to the
677 errors in surface emissivity correction (Duan et al., 2017; Wan, 2014; Lei et al., 2018). In the
678 present analysis, we found an overestimation error of MODIS T_s in the range of 0.5 – 1.5 K when
679 compared with *in-situ* infrared temperature measurements at the tropical savanna site. As
680 mentioned in section 3.1, a positive (negative) bias in T_s would tend to an overestimation
681 (underestimation) of amplitude (A) in eq. (5); underestimation (overestimation) of M in eq. (13),
682 and consequent underestimation (overestimation) of Γ (eq. 12) and G_i , respectively. Furthermore,
683 the standard deviation of NDVI surrounding the tower sites varied from 0.01 – 0.05 when
684 compared to the ground measurements, which could be another source of error in the STIC-TI
685 model. In addition, NDVI saturates at LAI > 3. However, STIC-TI provides direct estimates of
686 ecosystem G and is independent of R_N .

687 Despite the comparable accuracy of current G estimates with the G model of Bastiaanssen et al
688 (1998), the foundation of STIC-TI lies in the use of soil moisture characteristics with varying soil
689 textural types which are known to influence the soil heat conductance and thereby G. Thus, the
690 control of soil moisture on evaporation is explicitly included in STIC-TI as opposed to the semi-
691 empirical G function of Bastiaanssen et al (1998). The higher accuracies of TI-based thermal
692 diffusion model as compared to R_N -based empirical G models were also reported by Purdy et al.
693 (2016) at daily or longer time scales in cropland, grassland. All these G model estimates many a

694 times differ from in situ measurements because of the no accounting of leaf litter presence or layer
695 on soil floor in the remote sensing-based G-model.

696 The overestimation (underestimation) of $LE_i(H_i)$ is also due to the effects of spatial resolution of
697 different input variables on these two SEB fluxes and conducted statistical evaluation with respect
698 to the measured SEB fluxes. Eswar et al. (2017) demonstrated the need for spatial disaggregation
699 models for monitoring LE_i at field scale using contextual models by disaggregation of evaporative
700 fraction (Λ) and downwelling shortwave radiation ratio (R_G). Using different disaggregation
701 models, they estimated LE_i at 250m spatial resolution and reported RMSE of $30 - 32 \text{ W m}^{-2}$ as
702 compared to LE_i obtained at 1000m spatial resolution with RMSE of $40 - 70 \text{ Wm}^{-2}$ over different
703 sites in India. Anderson et al. (2007) reviewed different validation experiments conducted in
704 diverse agricultural landscapes (Anderson et al., 2004, 2005; Norman et al., 2003) and reported
705 RMSE in LE_i in the range of $35 - 40 \text{ W m}^{-2}$ (15%) at $30 - 120 \text{ m}$ disaggregated spatial resolution.
706 Current analysis also brought out the need for noon-night thermal imaging with spatial resolution
707 finer than 1000m to adequately capture the magnitude and variability of LE_i in the terrestrial
708 ecosystems especially agroecosystems where average field sizes are less ($< 0.5 \text{ ha}$) and fragmented
709 such as in India and other sub-continent.

710 As seen in Fig. 8a and Table 5, there is a gross overestimation of LE_i with respect to the tower
711 observations when MYD11A2 LST was used. The consistent positive BIAS in STIC-TI LE_i in
712 five out of nine sites is presumably due to the overestimation of R_{Ni} (Figure B1 of Appendix B)
713 and underestimation of G_i . Figure 7 shows overestimation of G_i for three OzFlux sites and US sites
714 and underestimation of G_i for Indian site with $G_i(\text{STIC-TI}) = 0.90 G_i(\text{tower}) - 0.10$ and
715 overestimation of R_{Ni} at the ecosystem-scale, with $R_{Ni}(\text{STIC-TI}) = 0.78R_{Ni}(\text{tower}) + 58.92$
716 (Appendix-B2). This means a systematic overestimation of net available energy ($R_{Ni} - G_i$) will be
717 obvious in cases where STIC-TI shows underestimation of G_i . [Since available energy is an](#)
718 [important component for estimating LE through the PMEB equation, an overestimation of net](#)
719 [available energy leads to an overestimation of LE by STIC-TI. Sensible heat flux will be](#)
720 [consequently underestimated due to the complementary nature of the PMEB equation. which](#)
721 [consequently leads to an overestimation of retrieved \$LE_i\$.](#) It may be also noted that the use of
722 MYD21A2 LST led to relatively better accuracy in LE_i (3-8%) and H_i (2-3%) as compared to
723 using MYD11A2 LST in semi-arid and arid ecosystems. The higher retrieval accuracy of
724 MYD21A2 LST using TES (Temperature-Emissivity Separation) algorithm over MYD11A2 LST

725 that uses split-window algorithm (Wan et al, 2015) is the main reason for obtaining higher accuracy
726 in LE_i and H_i estimates.

727 The standard deviations of MODIS Aqua day-night overpass time over study sites were found to
728 be within 30-45 minutes (Sharifnezhadazizi et al, 2019) and the expected deviation in LST from
729 the mean local time would be around $\pm 0.75K$ (Sharifnezhadazizi et al, 2019). Sensitivity analysis
730 showed that resultant uncertainties in STIC-TI heat flux estimates would be of the order of $\pm 5-7\%$
731 due to this LST uncertainty.

732 **5.3 Effects of SEB closure**

733 Given there is a widespread lack of SEB closure ($H + LE \neq R_N - G$) or residual energy balance,
734 knowledge of the impact of different vegetation types and climatic variables on SEB ‘non-closure’
735 is essential. A recent study by Dare-Idowu et al. (2021) covering 8 growing seasons and 3 crops
736 (maize, wheat, and rapeseed) in two sites of south-western France showed that the systematic effect
737 of each site on SEB closure was stronger than the influence of crop type and stage. Same study
738 revealed a greater percentage of SEB closure under unstable atmospheric conditions and in the
739 prevailing wind directions, and sensible heat advection accounted for more than half of the
740 imbalance at both the sites.

741 In our study, using unclosed SEB observations for Indian sites in the absence of *in-situ* G_i
742 observations also added to the consistent positive BIAS in the statistical evaluation of LE_i . A
743 ubiquitous lack of energy balance closure to the order of 10 – 20% worldwide at most of the EC
744 sites is reported in different literatures (Stoy et al., 2013; Wilson et al., 2002), which implies a
745 systematic underestimation (overestimation) of LE_i (EC tower) (and/or H_i (EC tower)).
746 Accommodating an average 15% imbalance in LE_i (EC tower) would tend to diminish the positive
747 BIAS in STIC-TI. Therefore, the pooled gain (0.98) and positive BIAS between the STIC-TI and
748 tower LE_i is determined by the overestimation of $(R_{Ni} - G_i)$, combined with the underestimation
749 of measured LE_i from the EC towers. An underestimation of H_i (negative BIAS) is associated with
750 two reasons; (a) ignoring the two-sided aerodynamic conductance of the leaves (Jarvis and
751 McNaughton, 1986; Monteith and Unsworth, 2013; Schymanski et al., 2017), which could lead to
752 substantial underestimation of H_i , and (b) due to the complementary nature of the PMEB equation,
753 if LE_i is overestimated, H_i will be underestimated. In addition, frequent micro-advection fluxes
754 alter measured in situ H and LE fluxes. But these advection conditions are not explicitly accounted

755 in the current STIC-TI model. At the EC tower sites, the fraction of residual energy balance to R_N
756 can be quantified with respect to vegetation/crop growth characteristics or biophysical properties.
757 However, where G observations are lacking such as in many Indian EC tower sites, the TI-based
758 G model can be used to fill up the missing G observations to quantify residual energy balance and
759 to correct the SEB non-closure.

760 **6 Summary and conclusions**

761 This study addressed one of the long-term uncertainties in thermal remote sensing of evaporation
762 modeling in open canopy heterogeneous ecosystems, which is associated with empirical methods
763 of estimating ground heat flux. We demonstrated for the first-time physical integration and
764 coupling of a mechanistic ground heat flux model with an analytical evaporation model (Surface
765 Temperature Initiated Closure, STIC) within the surface energy balance equation. The model is
766 called STIC-TI, which uses satellite-based land surface temperature from MODIS Aqua and
767 associated biophysical variables, and it has minimal independence on *in-situ* measurements. The
768 estimation of evaporation through STIC-TI does not require any empirical function for inferring
769 the biophysical conductances. STIC-TI is independent of uncertain parameterizations of surface
770 roughness and atmospheric stability and does not also involve any look-up table for biome or plant
771 functional attributes. By linking noon-night land surface temperature with harmonics equation of
772 thermal inertia and soil moisture availability, STIC-TI derived the ground heat flux, and
773 subsequently coupled it with evaporation. Independent validation of STIC-TI with respect to eddy
774 covariance flux measurements using measured flux data from nine terrestrial ecosystems in arid,
775 semi-arid and sub-humid climate in India, USA (~~representing northern hemisphere~~) and Australia
776 (~~representing southern hemisphere~~) led us to the following conclusions:

- 777 (i) While the MODIS Aqua day-night view angle difference showed strong impact on ground
778 heat flux and sensible heat flux estimate deviations of STIC-TI (with respect to
779 measurements), relatively weak dependence of latent heat flux errors on the day-night view
780 angle difference was noted.
- 781 (ii) ~~G estimates through STIC-TI performed better as compared to most of the contemporary~~
782 ~~empirical G models, with lower MAPD and higher correlation coefficient with respect to *in-*~~
783 ~~*situ* measurements.~~ The most notable advantages of STIC-TI are firstly, (a) it provides direct

784 estimates of ~~G~~ ground heat flux and is not dependent on net radiation estimates while
785 simultaneously integrates the effects of soil water stress on ground heat flux and evaporation
786 through the inclusion noon-night land surface temperature information. Secondly, ~~(b)~~ the
787 ecosystem-scale surface soil temperature amplitude used in ~~G~~ the ground heat flux model can
788 advance our understanding on associated terrestrial ecosystem processes.

789 ~~(iii) Underestimation of G in some ecosystems was primarily attributed to the inherent bias in~~
790 ~~MODIS T_s product, NDVI saturation at higher LAI (>3) in conjunction with the spatial scale~~
791 ~~mismatch between single MODIS pixel and the footprint of G measurements. The consequent~~
792 ~~overestimation (underestimation) of LE (H) in some ecosystems was associated with the~~
793 ~~overestimation of net available energy, use of ‘unelosed’ SEB observation in LE and H~~
794 ~~validation, the spatial scale discrepancy between MODIS pixel versus eddy covariance~~
795 ~~measurement footprint, the complementary nature of the Penman Monteith Energy Balance~~
796 ~~equation (for H), and possibly due to ignoring the two-sided aerodynamic conductance by the~~
797 ~~leaves (for H), respectively.~~

798 The requirement of few input variables in STIC-TI generates promise for surface-atmosphere
799 exchange studies using readily available data from the current generation remote sensing satellites
800 (e.g., MODIS, ~~INSATVIIRS~~) that have noon-night ~~TIR~~ land surface temperature observations.
801 STIC-TI can also be potentially used for distributed ET mapping using from current and future 4th
802 generation Indian Geostationary satellite observations from INSAT as well as future high spatial
803 resolution (~ 50 – 60 m) TIR missions having noon-night observations with 3-day high revisit from
804 polar orbiting platform (Lagouarde et al., 2018, 2019) through such as the planned Indo-French
805 space-borne mission, TRISHNA (Thermal infrared Imaging Satellite for High-resolution Natural
806 Resource Assessment) (Lagouarde et al., 2018, 2019), ESA’s LSTM (Land Surface Temperature
807 Monitoring), and NASA SBG (Surface Biology and Geology), respectively. This simple approach
808 will also help in catering the need for a reliable, space-time continuous ET datasets in data-poor
809 regions like Indian sub-tropics, South-East Asia, and other parts of the world from thermal remote
810 sensing observation.

811 **Author contributions**

812 KM and BKB conceptualized the idea; DD conducted STIC-TI model coding, simulations; BKB
813 and DD conducted the data analysis in consultation with KM; DD and BKB wrote the first version
814 of the manuscript with KM writing the introduction, discussions, and conclusions; BKB and KM
815 conducted all the analysis and writing during revision; all authors contributed to discussions,
816 editing and corrections; BKB and KM jointly finalized the manuscript.

817 **Acknowledgement**

818 The authors gratefully acknowledge Ministry of Earth Sciences (MoES), Govt. of India and
819 National Environmental Research Council for providing necessary support through Indo-UK
820 INCOMPASS programme (NE/L013819/1, NE/L013843/1, NE/L01386X/1, NE/P003117/1).
821 BKB acknowledges Deputy Director, EPSA, SAC-ISRO and Director, SAC-ISRO for providing
822 necessary support to participate and contribute to Indo-UK INCOMPASS programme. DD
823 acknowledges Prof. P.D. Lele and Head from Department of Physics, Electronics and Space
824 Sciences, Gujarat University Ahmedabad and for providing the necessary support to carry out this
825 work. KM was supported through the International Mobility fellowship of Luxembourg National
826 Research Fund (FNR) (INTER/MOBILITY/2020/14521920/MONASTIC). KCN is supported
827 by the Jet Propulsion Laboratory, California Institute of Technology, under contract with the
828 National Aeronautics and Space Administration and Government sponsorship is acknowledged.
829 DDB acknowledges support from NASA Ecostress project and the US Department of Energy,
830 Office of Science which supports the AmeriFlux project

831 **Data and code availability**

832 Harmonized time series datasets over the study grids are available in
833 <https://doi.org/10.5281/zenodo.5806501>. The model code is available to the first author upon
834 reasonable request.

835

836 **References**

- 837 Anderson, M., Kustas, W., Alfieri, J., Gao, F., Hain, C., Prueger, J., Evett, S., Colaizzi, P., Howell,
838 T. and Chávez, J.: Mapping daily evapotranspiration at Landsat spatial scales during the
839 BEAREX'08 field campaign, *Adv. Water Resour.*, 50, 162 – 177,
840 <https://doi.org/10.1016/j.advwatres.2012.06.005>, 2012.
- 841 Anderson, M., Norman, J., Kustas, W., Li, F., Prueger, J. and Mecikalski, J.: Effects of Vegetation
842 Clumping on Two-Source Model Estimates of Surface Energy Fluxes from an Agricultural
843 Landscape during SMACEX, *J. Hydrometeorol.*, 6(6), 892 – 909,
844 <https://doi.org/10.1175/JHM465.1>, 2005.
- 845 Anderson, M., Norman, J., Mecikalski, J., Otkin, J. and Kustas, W.: A climatological study of
846 evapotranspiration and moisture stress across the continental United States based on thermal
847 remote sensing: 1. Model formulation, *J. Geophys. Res.: Atmos.*, 112(D10),
848 <https://doi.org/10.1029/2006JD007506>, 2007.
- 849 Anderson, M., Norman, J., Mecikalski, J., Torn, R., Kustas, W. and Basara, J.: A Multiscale
850 Remote Sensing Model for Disaggregating Regional Fluxes to Micrometeorological Scales, *J.*
851 *Hydrometeorol.*, 5(2), 343 – 363, [https://doi.org/10.1175/1525-7541\(2004\)005<0343:AMRSMF>2.0.CO;2](https://doi.org/10.1175/1525-7541(2004)005<0343:AMRSMF>2.0.CO;2), 2004.
- 853 Bai, Y., Zhang, S., Bhattarai, N., Mallick, K., Liu, Q., Tang, L., Im, J., Guo, L., and Zhang, J: On
854 the use of machine learning based ensemble approaches to improve evapotranspiration
855 estimates from croplands across a wide environmental gradient, *Agric. Forest Meteorol.*, 298
856 - 299, 108308, <https://doi.org/10.1016/j.agrformet.2020.108308>, 2021.
- 857 Bastiaanssen, W. G. M., Menenti, M., Feddes, R. A. and Holtslag, A. A. M.: A remote sensing
858 surface energy balance algorithm for land (SEBAL). 1. Formulation, *J. Hydrol.*, 198 – 212,
859 doi:10.1016/S0022-1694(98)00253-4,1998.
- 860 Bennett, W., Wang, J. and Bras, R.: Estimation of Global Ground Heat Flux, *J. Hydrometeorol.*,
861 9(4), 744 – 759, <https://doi.org/10.1175/2008JHM940.1>, 2008.
- 862 Beringer, J., Hutley, L. B., McHugh, I., Arndt, S. K., Campbell, D., Cleugh, H. A., Cleverly, J.,
863 Resco de Dios, V., Eamus, D., Evans, B., Ewenz, C., Grace, P., Griebel, A., Haverd, V.,
864 Hinko-Najera, N., Huete, A., Isaac, P., Kanniah, K., Leuning, R., Liddell, M. J., Macfarlane,
865 C., Meyer, W., Moore, C., Pendall, E., Phillips, A., Phillips, R. L., Prober, S. M., Restrepo-
866 Coupe, N., Rutledge, S., Schroder, I., Silberstein, R., Southall, P., Yee, M. S., Tapper, N. J.,

867 van Gorsel, E., Vote, C., Walker, J., and Wardlaw, T.: An introduction to the Australian and
868 New Zealand flux tower network – OzFlux, *Biogeosciences*, 13, 5895–5916, doi:10.5194/bg-
869 13-5895-2016, 2016.

870 Bhat, G., Morrison, R., Taylor, C., Bhattacharya, B., Paleri, S., Desai, D., Evans, J., Pattnaik, S.,
871 Sekhar, M., Nigam, R., Sattar, A., Angadi, S., Kancha, D., Patidar, A., Tripathi, S., Krishnan,
872 K. and Sisodiya, A.: Spatial and temporal variability in energy and water vapor fluxes
873 observed at seven sites on the Indian subcontinent during 2017, *Q. J. R. Meteorolog. Soc.*, 146
874 (731), <https://doi.org/10.1002/qj.3688>, 2853 – 2866, 2019.

875 Bhattarai, N., Mallick, K., Brunzell, N. A., Sun, G., and Jain, M.: Regional evapotranspiration
876 from an image-based implementation of the Surface Temperature Initiated Closure (STIC1.2)
877 model and its validation across an aridity gradient in the conterminous US, *Hydrol. Earth Syst.*
878 *Sci.*, 22, 2311–2341, <https://doi.org/10.5194/hess-22-2311-2018>, 2018.

879 Bhattarai, N., Mallick, K., Stuart, J., Vishwakarma, B., Niraula, R., Sen, S. and Jain, M.: An
880 automated multi-model evapotranspiration mapping framework using remotely sensed and
881 reanalysis data, *Remote Sens. Environ.*, 229, 69 – 92,
882 <https://doi.org/10.1016/j.rse.2019.04.026>, 2019.

883 Boegh, E., Soegaard, H., Christensen, J. H., Hasager, C. B., Jensen, N.O. and Nielsen, N. W.:
884 Combining weather prediction and remote sensing data for the calculation of
885 evapotranspiration rates: application to Denmark, *Int. J. Remote Sens.*, 25, 2553 – 2574,
886 <https://doi.org/10.1080/01431160310001647984>, 2004.

887 Cammalleri, C. and Vogt, J.: On the Role of Land Surface Temperature as Proxy of Soil Moisture
888 Status for Drought Monitoring in Europe, *Remote Sens.*, 7(12), 16849 – 16864,
889 <https://doi.org/10.3390/rs71215857>, 2015.

890 Cano, D., Monget, J., Albuissou, M., Guillard, H., Regas, N. and Wald, L.: A method for the
891 determination of the global solar radiation from meteorological satellite data. *Solar Energy*,
892 37(1), 840, 31 – 39, [https://doi.org/10.1016/0038-092X\(86\)90104-0](https://doi.org/10.1016/0038-092X(86)90104-0), 1986.

893 Castelli, F., Entekhabi, D. and Caporali, E.: Estimation of surface heat flux and an index of soil
894 moisture using adjoint-state surface energy balance, *Water Resour. Res.*, 35(10), 3115 – 3125,
895 <https://doi.org/10.1029/1999WR900140>, 1999.

896 Dare-Idowu, O., Brut, A., Cuxart, J., Tallec, T., Rivalland, V., Zawilski, B., Ceschia, E. and

897 Jarlan, L.: Surface energy balance and flux partitioning of annual crops in south-western
898 France. *Agric. For. Meteorol.*, 308 – 309, 108529,
899 <https://doi.org/10.1016/j.agrformet.2021.108529>, 2021.

900 Didan, K.: MOD13Q1 MODIS/Terra Vegetation Indices 16-Day L3 Global 250m SIN Grid
901 V006., distributed by NASA EOSDIS Land Processes DAAC,
902 doi:10.5067/MODIS/MOD13Q1.006, 2021-06-06, 2015.

903 Donohue, R. J., Hume, I. H., Roderick, M. L., McVicar, T. R., Beringer, J., Hutley, L. B., Arndt,
904 S. K.: Evaluation of the remote-sensing-based DIFFUSE model for estimating photosynthesis
905 of vegetation, *Remote Sens. Environ.*, 155, 349–365, doi:10.1016/j.rse.2014.09.007, 2014.

906 Duan, A., Wang, M., Lei, Y. and Cui, Y.: Trends in summer rainfall over China associated with
907 the Tibetan Plateau sensible heat source during 1980–2008, *J. Clim.*, 26, 261–275,
908 <https://doi.org/10.1175/JCLI-D-11-00669.1>, 2013.

909 Duan, S., Li, Z., Cheng, J. and Leng, P.: Cross-satellite comparison of operational land surface
910 temperature products derived from MODIS and ASTER data over bare soil surfaces. *ISPRS*
911 *J. Photogramm. Remote Sens.*, 126, 1-10, <https://doi.org/10.1016/j.isprsjprs.2017.02.003>,
912 2017.

913 Eswar, R., Sekhar, M., Bhattacharya, B. and Bandyopadhyay, S.: Spatial Disaggregation of Latent
914 Heat Flux Using Contextual Models over India, *Remote Sens.*, 9(9), 949,
915 <https://doi.org/10.3390/rs9090949>, 2017.

916 Friedl, M., McIver, D., Hodges, J., Zhang, X., Muchoney, D., Strahler, A., Woodcock, C., Gopal,
917 S., Schneider, A., Cooper, A., Baccini, A., Gao, F. and Schaaf, C.: Global land cover mapping
918 from MODIS: algorithms and early results, *Remote Sens. Environ.*, 83(1-2), 287 – 302,
919 [https://doi.org/10.1016/S0034-4257\(02\)00078-0](https://doi.org/10.1016/S0034-4257(02)00078-0), 2002.

920 Gao, Z., Horton, R. and Liu, H. P.: Impact of wave phase difference between soil surface heat flux
921 and soil surface temperature on soil surface energy balance closure, *J. Geophys. Res.*, 115,
922 D16112, doi:10.1029/2009JD013278, 2010.

923 Hillel, D.: *Introduction to Soil Physics*, San Diego, US, ISBN 9780123485205, 1982.

924 Hulley, G., Malakar, N., and Freepartner, R.: Moderate Resolution Imaging Spectroradiometer
925 (MODIS) Land Surface Temperature and Emissivity Product (MxD21) Algorithm Theoretical
926 Basis Document Collection-6. Pasadena, California: Jet Propulsion Laboratory, California
927 Institute of Technology, 2016

928 Isaac, P., Cleverly, J., McHugh, I., van Gorsel, E., Ewenz, C., and Beringer, J.: OzFlux data:
929 network integration from collection to curation, *Biogeosciences*, 14, 2903–2928,
930 doi:10.5194/bg-14-2903-2017, 2017.

931 Jarvis, P.G. and McNaughton, K.G.: Stomatal Control of Transpiration – Scaling up from Leaf to
932 Region, *Adv. Ecol. Res.*, 15, 1-49, [https://doi.org/10.1016/S0065-2504\(08\)60119-1](https://doi.org/10.1016/S0065-2504(08)60119-1), 1986.

933 Johansen, O.: Thermal conductivity of soils, PhD Thesis, University of Trondheim. Hanover, NH:
934 Cold Regions Research and Engineering Laboratory, US Army Corps of Engineers, CRREL
935 Draft English translation, <https://apps.dtic.mil/sti/pdfs/ADA044002.pdf>, 1975.

936 Johnston, M., Andreu, A., Verfaillie, J., Baldocchi, D., and Moorcroft, P.: What lies beneath:
937 Vertical temperature heterogeneity in a Mediterranean woodland savanna, *Remote Sens.*
938 *Environ.*, <https://doi.org/10.1016/j.rse.2022.112950>, 2022.

939 Kiptala, J., Mohamed, Y., Mul, M. and Van der Zaag, P.: Mapping evapotranspiration trends using
940 MODIS and SEBAL model in a data scarce and heterogeneous landscape in Eastern
941 Africa, *Water Resour. Res.*, 49(12), 8495 – 8510, <https://doi.org/10.1002/2013WR014240>,
942 2013.

943 Kustas, W. and Anderson, M.: Advances in thermal infrared remote sensing for land surface
944 modeling, *Agric. For. Meteorol.*, 149 (12), 2071 – 2081,
945 <https://doi.org/10.1016/j.agrformet.2009.05.016>, 2009.

946 Lagouarde J.-P., Bhattacharya BK, Crébassol P., Gamet P., Babu SS, Boulet G., Briottet X.,
947 Buddhiraju KM, Cherchali S., Dadou I., Dedieu G., Gouhier M., Hagolle O Irvine M., Jacob
948 F., Kumar A., Kumar KK, Laignel B., Mallick K., Murthy CS, Olioso A., Otlé C., Pandya
949 MR, Raju PV, Roujean J.-L., Sekhar M., Shukla MV, Singh SK, Sobrino J., Ramakrishnan
950 R.: The Indian-French Trishna Mission: Earth Observation in the Thermal Infrared with High
951 Spatio-Temporal Resolution, IGARSS 2018 - 2018 IEEE International Geoscience and
952 Remote Sensing Symposium, Institute of Electrical and Electronics Engineers (IEEE). USA,
953 4078-4081, doi:10.1109/IGARSS.2018.8518720, 2018.

954 Lagouarde, J., Bhattacharya, B., Crébassol, P., Gamet, P., Adlakha, D., Murthy, C., Singh, S.,
955 Mishra, M., Nigam, R., Raju, P., Babu, S., Shukla, M., Pandya, M., Boulet, G., Briottet, X.,
956 Dadou, I., Dedieu, G., Gouhier, M., Hagolle, O., Irvine, M., Jacob, F., Kumar, K., Laignel,
957 B., Maisongrande, P., Mallick, K., Olioso, A., Otlé, C., Roujean, J., Sobrino, J.,
958 Ramakrishnan, R., Sekhar, M. and Sarkar, S.: Indo-French high-resolution thermal infrared

959 space mission for earth natural resources assessment and monitoring – concept and definition
960 of TRISHNA, ISPRS - International Archives of the Photogrammetry, Remote Sensing and
961 Spatial Information Sciences, XLII-3/W6, 403-407, 2019.

962 Lu, L., Zhang, T., Wang, T. and Zhou, X.: Evaluation of Collection-6 MODIS Land Surface
963 Temperature Product Using Multi-Year Ground Measurements in an Arid Area of Northwest
964 China, *Remote Sens.*, 10(11), 1852, <https://doi.org/10.3390/rs10111852>, 2018.

965 Mallick, K.,& Bhattacharya, B.K., Chaurasia, S., Dutta, S., Nigam, R., Mukherjee J., Banerjee,
966 S., Kar, G., Rao, V., Gadgil, A., Parihar, J.: Evapotranspiration using MODIS data and limited
967 ground observations over selected agroecosystems in India, *Int. J. Remote Sens.*, 28 (10),
968 2091 – 2110, <https://doi.org/10.1080/01431160600935620>, 2007.

969 Mallick, K., Bhattacharya, B. K., Rao, V. U. M., Reddy, D.R., Banerjee, S., Venkatesh, H. ,
970 Pandey, V., Kar, G., Mukherjee, J., Vyas, S., Gadgil, A.S., Patel, N.K.: Latent heat flux
971 estimation in clear sky days over Indian agroecosystems using noontime satellite remote
972 sensing data, *Agric. For. Meteorol.*, 149 (10), 1646 – 1665,
973 <https://doi.org/10.1016/j.agrformet.2009.05.006>, 2009.

974 Mallick, K., Boegh, E., Trebs, I., Alfieri, J., Kustas, W., Prueger, J., Niyogi, D., Das, N., Drewry,
975 D., Hoffmann, L. and Jarvis, A.: Reintroducing radiometric surface temperature into the
976 Penman-Monteith formulation, *Water Resour. Res.*, 51(8), 6214 – 6243,
977 <https://doi.org/10.1002/2014WR016106>, 2015a.

978 Mallick, K., Jarvis, A., Boegh, E., Fisher, J., Drewry, D., Tu, K., Hook, S., Hulley, G., Ardö, J.,
979 Beringer, J., Arain, A. and Niyogi, D.: A Surface Temperature Initiated Closure (STIC) for
980 surface energy balance fluxes, *Remote Sens. Environ.*, 141, 243 – 261,
981 <https://doi.org/10.1016/j.rse.2013.10.022>, 2014.

982 Mallick, K., Jarvis, A., Wohlfahrt, G., Kiely, G., Hirano, T., Miyata, A., Yamamoto, S., and
983 Hoffmann, L.: Components of near-surface energy balance derived from satellite soundings –
984 Part 1: Noontime net available energy, *Biogeosci.*, 12, 433–451, [https://doi.org/10.5194/bg-](https://doi.org/10.5194/bg-12-433-2015)
985 12-433-2015, 2015b.

986 Mallick, K., Toivonen, E., Trebs, I., Boegh, E., Cleverly, J., Eamus, D., Koivusalo, H., Drewry,
987 D., Arndt, S., Griebel, A., Beringer, J. and Garcia, M.: Bridging thermal infrared sensing and
988 physically-based evapotranspiration modeling: from theoretical implementation to validation

989 across an aridity gradient in Australian ecosystems, *Water Resour. Res.*, 54 (5), 3409 – 3435,
990 <https://doi.org/10.1029/2017WR021357>, 2018a.

991 Mallick, K., Trebs, I., Boegh, E., Giustarini, L., Schlerf, M., Drewry, D., Hoffmann, L., von
992 Randow, C., Kruijt, B., Araùjo, A., Saleska, S., Ehleringer, J., Domingues, T., Ometto, J.,
993 Nobre, A., de Moraes, O., Hayek, M., Munger, J. and Wofsy, S.: Canopy-scale biophysical
994 controls of transpiration and evaporation in the Amazon Basin, *Hydrol. Earth Syst. Sci.*, 20,
995 4237 – 4264, doi:10.5194/hess-20-4237-2016, 2016.

996 Mallick, K., Wandera, L., Bhattarai, N., Hostache, R., Kleniewska, M. and Chormanski, J.: A
997 Critical Evaluation on the Role of Aerodynamic and Canopy–Surface Conductance
998 Parameterization in SEB and SVAT Models for Simulating Evapotranspiration: A Case Study
999 in the Upper Biebrza National Park Wetland in Poland, *Water*, 10 (12), 1753,
1000 <https://doi.org/10.3390/w10121753>, 2018b.

1001 Mallick, K., Baldocchi, D., Jarvis, A., Hu, T., Trebs, I., Sulis, M., et al.: Insights into the
1002 aerodynamic versus radiometric surface temperature debate in thermal-based evaporation
1003 modeling. *Geophys. Res. Lett.*, 49, e2021GL097568. <https://doi.org/10.1029/2021GL097568>,
1004 2022.

1005 Maltese, A., Bates, P., Capodici, F., Cannarozzo, M., Ciraolo, G. and La Loggia, G.: Critical
1006 analysis of thermal inertia approaches for surface soil water content retrieval, *Hydrol. Sci. J.*,
1007 58(5), 1144 – 1161, <https://doi.org/10.1080/02626667.2013.802322>, 2013.

1008 Martel, M., Glenn, A., Wilson, H. and Kröbel, R.: Simulation of actual evapotranspiration from
1009 agricultural landscapes in the Canadian Prairies, *J. Hydrol. Reg. Stud.*, 15, 105 – 118,
1010 <https://doi.org/10.1016/j.ejrh.2017.11.010>, 2018.

1011 Matheny, A., Bohrer, G., Stoy, P., Baker, I., Black, A., Desai, A., Dietze, M., Gough, C., Ivanov,
1012 V., Jassal, R., Novick, K., Schäfer, K. and Verbeeck, H.: Characterizing the diurnal patterns
1013 of errors in the prediction of evapotranspiration by several land-surface models: An NACP
1014 analysis, *J. Geophys. Res. Biogeosci.*, 119 (7), 1458 – 1473,
1015 <https://doi.org/10.1002/2014JG002623>, 2014.

1016 Minasny, B. & Hartemink, A. E.: Predicting soil properties in the tropics. *Earth-Science Rev.*, 1 –
1017 2, 52 – 62, <https://doi.org/10.1016/j.earscirev.2011.01.005>, 2011.

1018 Mihailovic, D. T., Kallos, G., Aresenic, I.D., Lalic, B., Rajkovic, B. and Papadopoulos, A.:
1019 Sensitivity of soil surface temperature in a Force-Restore Equation to heat fluxes and deep
1020 soil temperature. *Intl. J. Climatol.*, 19, 1617 – 1632, 1999.

1021 Monteith, J & Unsworth, M.: *Principles of Environmental Physics: Plants, Animals, and the*
1022 *Atmosphere*, Fourth Edition, 1-401, 2013.

1023 Moran, M. S., Jackson, R. D., Raymond, L. H., Gay, L. W. and Slater, P. N.: Mapping surface
1024 energy balance components by combining landsat thematic mapper and ground-based
1025 meteorological data, *Remote Sens. Environ.*, 30, 77 – 87, [https://doi.org/10.1016/0034-](https://doi.org/10.1016/0034-4257(89)90049-7)
1026 [4257\(89\)90049-7](https://doi.org/10.1016/0034-4257(89)90049-7), 1989.

1027 Morisson, R., Angadi, S. S., Cooper, H. M., Evans, J. G., Rees, G., Sekhar, M., Taylor, C.,
1028 Tripathi, S. N. and Turner, A. G. : Energy and carbon dioxide fluxes, meteorology and soil
1029 physics observed at INCOMPASS land surface stations in India, 2016 to 2017, NERC
1030 Environmental Information Data Centre, doi:10.5285/78c64025-1f8d-431cbdeb-
1031 e69a5877d2ed, 2019b.

1032 Morisson, R., Angadi, S. S., Cooper, H. M., Evans, J., Rees, G., Sekhar, M., Taylor, C., Tripathi,
1033 S. N. and Turner, A. G. : High temporal resolution meteorology and soil physics observations
1034 from INCOMPASS land surface stations in India, 2016 to 2018, NERC Environmental
1035 Information Data Centre, doi:10.5285/c5e72461-c61f-4800-8bbf-95c85f74c416, 2019a.

1036 Murray, T. and Verhoef, A.: Moving towards a more mechanistic approach in the determination
1037 of soil heat flux from remote measurements, *Agric. For. Meteorol.*, 147(1-2), 80 – 87,
1038 <https://doi.org/10.1016/j.agrformet.2007.06.009>, 2007.

1039 Norman, J., Anderson, M., Kustas, W., French, A., Mecikalski, J., Torn, R., Diak, G., Schmugge,
1040 T. and Tanner, B.: Remote sensing of surface energy fluxes at 10¹-m pixel resolutions, *Water*
1041 *Resour. Res.* 39(8), <https://doi.org/10.1029/2002WR001775>, 2003.

1042 Purdy, A., Fisher, J., Goulden, M. and Famiglietti, J.: Ground heat flux: An analytical review of
1043 6 models evaluated at 88 sites and globally, *J. Geophys. Res.: Biogeosci.*, 121(12), 3045 –
1044 3059, <https://doi.org/10.1002/2016JG003591>, 2016.

1045 Raja, P., Singh, M., Singh, N., and Sinha, N.K.: Photosynthesis and Biomass studies in
1046 *Lasiurus indicus* of Chandan Grassland in Thar Desert, XXIII International Grassland
1047 Conference, New Delhi, Volume: IGC 2015, 2015.

1048 Santanello, J. and Friedl, M.: Diurnal Covariation in Soil Heat Flux and Net Radiation, *J. Appl.*
1049 *Meteorol.*, 42(6), 851 – 862, [https://doi.org/10.1175/1520-](https://doi.org/10.1175/1520-0450(2003)042<0851:DCISHF>2.0.CO;2)
1050 [0450\(2003\)042<0851:DCISHF>2.0.CO;2](https://doi.org/10.1175/1520-0450(2003)042<0851:DCISHF>2.0.CO;2), 2003.

1051 Schmid, H.P.: Footprint modelling for vegetation atmosphere exchange studies: a review and
1052 perspective. *Agric. For. Meteorol.*, 113, 159 – 183, 2002.

1053 Sauer T.J. and Horton, R.: Soil Heat flux, *Micrometeorology in Agricultural Systems*, Agronomy
1054 Monograph no. 47, American Society of Agronomy, Crop Science Society of America, Soil
1055 Science Society of America, 677 S. Segoe Rd., Madison, WI 53711, USA, 2005.

1056 Schaaf, C., Gao, F., Strahler, A., Lucht, W., Li, X., & Tsang, T. , trugnell, N. C., Zhang, X., Jin,
1057 Y., Muller, J., Lewis, P., Barnsley, M., Hobson, P., Disney, M., Roberts, G., Dunderdale, M.,
1058 Doll, C., d'Entremont, R. P., Hu, B., Liang, S., Privette, J. L. and Roy, D. : First operational
1059 BRDF, albedo nadir reflectance products from MODIS, *Remote Sens. Environ.*, 83(1-2), 135
1060 – 148, doi:10.1016/s0034-4257(02)00091-3, 2002.

1061 Schymanski, S. J., Breitenstein, D., and Or, D.: Technical note: An experimental set-up to measure
1062 latent and sensible heat fluxes from (artificial) plant leaves, *Hydrol. Earth Syst. Sci.*, 21, 3377–
1063 3400, <https://doi.org/10.5194/hess-21-3377-2017>, 2017.

1064 Singh, A.: *Integrated Water Management: Water and Plant Growth*, 1–16, 2007.

1065 [Sharfinezhadazizi, Z., Nobouzi, H., Prakash, S., Beale, C., and Khanbilvardi, R.: A global analysis](#)
1066 [of land surface temperature diurnal cycle using MODIS observations, *J. Appl. Meteorol.*](#)
1067 [*Climatol.*, 58, 1279 – 1291, doi:10.1175/JAMC-D-18-0256.1, 2019.](#)

1068 Stoy, P., Mauder, M., Foken, T., Marcolla, B., Boegh, E., Ibrom, A., Arain, M., Arneth, A.,
1069 Aurela, M., Bernhofer, C., Cescatti, A., Dellwik, E., Duce, P., Gianelle, D., van Gorsel, E.,
1070 Kiely, G., Knohl, A., Margolis, H., McCaughey, H., Merbold, L., Montagnani, L., Papale, D.,
1071 Reichstein, M., Saunders, M., Serrano-Ortiz, P., Sottocornola, M., Spano, D., Vaccari, F. and
1072 Varlagin, A.: A data-driven analysis of energy balance closure across FLUXNET research
1073 sites: The role of landscape scale heterogeneity, *Agric. For. Meteorol.*, 171 – 172, 137 – 152,
1074 <https://doi.org/10.1016/j.agrformet.2012.11.004>, 2013.

1075 Su, Z.: The Surface Energy Balance System (SEBS) for estimation of turbulent heat fluxes,
1076 *Hydrol. Earth Syst. Sci.*, 6, 85–100, doi:10.5194/hess-6-85-2002, 2002.

1077 Tian, L., Zhang, Y., & Zhu, J.: Decreased surface albedo driven by denser vegetation on the
1078 Tibetan Plateau, *Environ. Res. Lett.*, 9 (10), 104001, doi:10.1088/1748-9326/9/10/104001,
1079 2014.

1080 Trebs, I., Mallick, K., Bhattarai, N., Sulis, M., Cleverly, J., Woodgate, W., Silberstein, R., Najera,
1081 H.-N., Beringer, J., Meyer, W. S., Su, Z., and Boulet, G.: The role of aerodynamic resistance
1082 in thermal remote sensing-based evapotranspiration models, *Remote Sens. Environ.*, 264,
1083 112602, doi:10.1016/j.rse.2021.112602, 2021

1084 Tsuang, B.: Ground Heat Flux Determination according to Land Skin Temperature Observations
1085 from *in-situ* Stations and Satellites, *J. Hydrometeorol.*, 6 (4), 371 – 390,
1086 <https://doi.org/10.1175/JHM425.1>, 2005.

1087 Turner, A., Bhat, G., Martin, G., Parker, D., Taylor, C., Mitra, A., Tripathi, S., Milton, S.,
1088 Rajagopal, E., Evans, J., Morrison, R., Pattnaik, S., Sekhar, M., Bhattacharya, B., Madan, R.,
1089 Govindankutty, M., Fletcher, J., Willetts, P., Menon, A. and Marsham, J.: Interaction of
1090 convective organization with monsoon precipitation, atmosphere, surface and sea: The 2016
1091 INCOMPASS field campaign in India, *Q. J. R. Meteorolog. Soc.*, 1–25,
1092 <https://doi.org/10.1002/qj.3633>, 2019.

1093 Van Dijk, A.I.J.M., Gash, J.H., Gorsel, E.V., Blanken, P.D., Cescatti, A., Emmel, C., Gielen, B.,
1094 Harman, I.N., Kiely, G., Merbold, L., Montagnani, L., Moors, E., Sottocornola, M., Varlagin,
1095 A., Williams, C.A., Wohlfahrt, G.: Rainfall interception and the coupled surface water and
1096 energy balance, *Agric For Meteorol.*, 214 – 215, 402 – 415,
1097 <https://doi.org/10.1016/j.agrformet.2015.09.006>, 2015.

1098 Van Genuchten, M.: A Closed-form Equation for Predicting the Hydraulic Conductivity of
1099 Unsaturated Soils, *Soil Sci. Soc. Am. J.*, 44 (5), 892,
1100 <https://doi.org/10.2136/sssaj1980.03615995004400050002x>, 1980.

1101 Venturini, V., Islam, S. and Rodriguez, L.: Estimation of evaporative fraction and
1102 evapotranspiration from MODIS products using a complementary based model, *Remote Sens.*
1103 *Environ.*, 112(1), 132 – 141, doi:10.1016/j.rse.2007.04.014, 2008.

1104 Verhoef, A., Otlé, C., Cappelaere, B., Murray, T., Saux-Picart, S., Zribi, M., Maignan, F.,
1105 Boulain, N., Demarty, J. and Ramier, D.: Spatio-temporal surface soil heat flux estimates from
1106 satellite data; results for the AMMA experiment at the Fakara (Niger) supersite, *Agric. For.*
1107 *Meteorol.*, 154-155, 55 – 66, doi:10.1016/j.agrformet.2011.08.003, 2012.

1108 Verhoef, A.: Remote estimation of thermal inertia and soil heat flux for bare soil, *Agric. For.*
1109 *Meteorol.*, 123(3-4), 221 – 236, doi:10.1016/j.agrformet.2003.11.005,2004.

1110 Vesala, T., Kljun, N., Rannik, U., Rinne, A. Sogachev, Markkanen, T., Sabelfeld, K., Foken, T.
1111 and Leclerc, M.Y.: Flux and concentration footprint modelling: State of the art. *Environ.*
1112 *Polln.*, 152, 653 – 666, 2008.

1113 Wan, Z.: New refinements and validation of the collection-6 MODIS land-surface
1114 temperature/emissivity product, *Remote Sens. Environ.*, 140, 36 – 45,
1115 doi:10.1016/j.rse.2013.08.027, 2014.

1116 Wang, S., Yang, Y., Luo, Y., and Rivera, A.: Spatial and seasonal variations in evapotranspiration
1117 over Canada's landmass, *Hydrol. Earth Syst. Sci.*, 17, 3561–3575, doi:10.5194/hess-17-3561-
1118 2013, 2013.

1119 Wilson, K., Goldstein, A., Falge, E., Aubinet, M., Baldocchi, D., Berbigier, P., Bernhofer, C.,
1120 Ceulemans, R., Dolman, H., Field, C., Grelle, A., Ibrom, A., Law, B., Kowalski, A., Meyers,
1121 T., Moncrieff, J., Monson, R., Oechel, W., Tenhunen, J., Valentini, R. and Verma, S.: Energy
1122 balance closure at FLUXNET sites, *Agric. For. Meteorol.*, 113(1-4), 223 – 243,
1123 doi:10.1016/S0168-1923(02)00109-0,2002.

1124 Winter, J. and Eltahir, E.: The Sensitivity of Latent Heat Flux to Changes in the Radiative Forcing:
1125 A Framework for Comparing Models and Observations, *J. Clim.*, 23(9),2345-2356,
1126 doi:10.1175/2009JCLI3158.1,2010.

1127 Zerefos, C. S. & Bais, A. F.: *Solar Ultraviolet Radiation: Modelling, Measurements and*
1128 *Effects*, Springer Berlin Heidelberg, 2013.

1129
1130
1131
1132
1133

Attributes	Symbol	Description
Temperature	T_A	Air temperature ($^{\circ}\text{C}$)
	T_{Max}	Maximum air temperature ($^{\circ}\text{C}$)
	T_{Min}	Minimum air temperature ($^{\circ}\text{C}$)
	T_D	Air dew-point temperature ($^{\circ}\text{C}$)
	T_{STA}	point-scale soil temperature amplitude
	ΔT_s	noon-night LST difference ($^{\circ}\text{C}$)
	T_{ST}	Soil temperature ($^{\circ}\text{C}$)
	T_s	Land surface temperature (LST) ($^{\circ}\text{C}$)
Humidity, vapor pressures	R_H	Relative humidity (%)
	e_A	Atmospheric vapor pressure at the level of T_A measurement (hPa)
	e_A^*	Saturation vapor pressure at the level of T_A measurement (hPa)
	e_s^*	Saturation vapor pressure at surface (hPa)
	D_A	Atmospheric vapor pressure deficit at the level of T_A measurement (hPa)
Radiation	R_G	Downwelling shortwave radiation (or global radiation) (W m^{-2})
	R_R	Upwelling or reflected shortwave radiation (W m^{-2})
	$R_{L\downarrow}$	Downwelling longwave radiation (W m^{-2})
	$R_{L\uparrow}$	Upwelling longwave radiation (W m^{-2})
	τ_{sw}	Atmospheric transmissivity for shortwave radiation (unitless)
	α_R	Broadband shortwave surface albedo (unitless)
SEB components	LE_i	Latent heat flux (W m^{-2}); subscript 'i' signifies 'instantaneous'
	H_i	Sensible heat flux (W m^{-2}); subscript 'i' signifies 'instantaneous'
	G_i	Ground heat flux (W m^{-2}); subscript 'i' signifies 'instantaneous'
	R_{N_i}	Net radiation (W m^{-2}); subscript 'i' signifies 'instantaneous'
	ϕ	Net available energy (W m^{-2}); i.e., $R_N - G$
	A	Ecosystem-scale surface soil temperature amplitude ($^{\circ}\text{C}$)

MV2007 model	T_{sd}	Daytime T_s ($^{\circ}\text{C}$)
	T_{sn}	Nighttime T_s ($^{\circ}\text{C}$)
	ω	Angular frequency (rad s^{-1})
	ϕ'_n	Phase shift of the n^{th} soil surface temperature harmonic (rad)
	Δ	Shape parameter (unitless)
	S_r	Relative soil moisture saturation ($\text{m}^3 \text{m}^{-3}$)
	f_s	Sand fraction (unitless)
	θ_{fc}	Soil water content at field capacity ($\text{m}^3 \text{m}^{-3}$)
	θ_{wp}	Soil water content at permanent wilting point ($\text{m}^3 \text{m}^{-3}$)
	θ^*	Soil porosity ($\text{cm}^3 \text{cm}^{-3}$)
	J_s	Summation of harmonic terms of soil surface temperature (K)
	Υ'	Soil textural parameter (unitless)
	Γ	Soil thermal inertia ($\text{J K}^{-1} \text{m}^{-2} \text{s}^{-0.5}$)
	τ_0	Thermal inertia of air-dry soil ($\text{J K}^{-1} \text{m}^{-2} \text{s}^{-0.5}$)
	τ^*	Thermal inertia of saturated soil ($\text{J K}^{-1} \text{m}^{-2} \text{s}^{-0.5}$)
	t'	Time of satellite overpass (seconds)
	Δt	Time offset between the canopy composite temperature and the below-canopy soil surface temperature (seconds)
	κ	Total number of harmonics used (unitless)
	f_c	Vegetation fraction (unitless)
	θ	Volumetric soil moisture (cm cm^{-3})
Clear-sky R_{Ni} model	R_{ns}	Net shortwave radiation (W m^{-2})
	R_{nl}	Net long wave radiation (W m^{-2})
	G_{sc}	Solar constant (1367 W m^{-2})
	β_e	Sun elevation angle ($^{\circ}$).
	ε_s	Infrared surface emissivity (unitless)
	ε_a	Atmospheric emissivity (unitless)
	E	Eccentricity correction factor due to variation in Sun-Earth distance (unitless)
	M	Aggregated moisture availability (0-1)

STIC-TI model	g_A	Aerodynamic conductance ($m s^{-1}$)
	g_s	Canopy-surface conductance ($m s^{-1}$)
	T_0	Aerodynamic temperature (or source/sink height temperature) ($^{\circ}C$)
	T_{0D}	Dewpoint temperature at the source/sink height ($^{\circ}C$)
	Λ	Evaporative fraction (unit less)
	e_0	Vapor pressure at the source/sink height (hPa)
	e_0^*	Saturation vapor pressure at the source/sink height (hPa)
	D_0	Vapor pressure deficit at source/sink height (hPa)
	s_1	Psychrometric slope of vapor pressure and temperature between ($T_{0D} - T_D$) versus ($e_0 - e_A$) ($h Pa K^{-1}$)
	s_2	Psychrometric slope of vapor pressure and temperature between ($T_s - T_D$) versus ($e_s^* - e_A$) ($h Pa K^{-1}$)
	s_3	Psychrometric slope of vapor pressure and temperature between ($T_{0D} - T_D$) versus ($e_s^* - e_A$).
	κ	Ratio between ($e_0^* - e_A$) and ($e_s^* - e_A$) (unitless)
	s	Slope of saturation vapor pressure vs. temperature curve ($h Pa K^{-1}$)
α	Priestley-Taylor coefficient (unitless)	
Ancillary meteorological variables	U	Wind speed at 8 m height ($m s^{-1}$)
	u^*	Friction velocity ($m s^{-1}$)
Constants	P	Precipitation ($mm d^{-1}$)
	γ	Psychrometric constant ($h Pa K^{-1}$)
	c_p	Specific heat capacity of air at constant pressure ($MJ kg^{-1} K^{-1}$)
	ρ	Density of air ($Kg m^{-3}$)
	σ	Stefan–Boltzmann constant ($5.67 \times 10^{-8} Wm^{-2}K^{-4}$)
<u>Sensor view geometry</u>	<u>VZA</u>	<u>MODIS Aqua sensor view angle ($^{\circ}$)</u>
	<u>δVZA</u>	<u>Difference in MODIS Aqua day-night sensor view angle ($^{\circ}$)</u>

1137 **Table A2:** Summary of instruments used, height or depth and period of measurements, measured
 1138 variables at nine EC flux tower sites

Type of primary instruments used for in situ data recording at flux tower sites	Measurement height/ depth (m)	Measured variables
Net radiometer	<ul style="list-style-type: none"> • 3m (IND-Naw, IND-Jai, IND-Sam) • 15m (AU-Ade) • 12.2m (AU-ASM) • 23m (AU-How) 2m (US-Ton, US-Var) 	Four radiation flux components: shortwave incoming (R_G) and outgoing (R_R); longwave incoming ($R_{L\downarrow}$) and outgoing ($R_{L\uparrow}$)
EC assembly with IRGA (Infrared Gas Analyzer), three-dimensional sonic anemometer, TC probe	<ul style="list-style-type: none"> • 8m (IND-Naw; IND-Jai; IND-Sam) • 4.5m (IND-Dha) • 15m (AU-Ade) • 11.6m (AU-ASM) • 23m (AU-How) • 2m (US-Ton, US-Var) 	High response wind vectors (u , v and w), sonic temperature, and CO_2 - water vapor mass at 10/20 Hz frequency
Humidity and temperature probe	<ul style="list-style-type: none"> • 8m (IND-Naw, IND-Jai, IND-Sam) • 4.5m (IND-Dha) • 15m (AU-Ade), 11.6m (AU-ASM) • 23m (AU-How), 70m (AU-How) • 2m (US-Ton, US-Var) 	T_A and R_H
Soil temperature probe	<ul style="list-style-type: none"> • -0.1m (IND-Dha) • -0.15m (AU-Ade) • (-0.02, -0.06m) (AU-ASM) • -0.08m (AU-How) • -0.02m, -0.04m, -0.08m, and -0.16m (US-Ton, US-Var) 	T_{ST}
Soil heat flux plates	<ul style="list-style-type: none"> • Ground, 0.1 m (IND-Dha) • Ground, -0.15 m (AU-Ade) • Ground, -0.08 m (AU-ASM) • Ground, -0.15 m (AU-How) • -0.01m (US-Ton, US-Var) 	Soil heat flux (G)

1139 **Appendix B**

1140 **B1: Clear-sky instantaneous net radiation (R_{Ni}) model**

1141 Net radiation (R_N) is defined as the difference between the incoming and outgoing radiation, which
 1142 includes both longwave and shortwave radiation at the Earth's surface.

1143 Terrestrial R_N has four components: downwelling and upwelling shortwave radiation (R_G and R_R),
 1144 downwelling and upwelling longwave radiation ($R_{L\downarrow}$ and $R_{L\uparrow}$), respectively.

$$R_N = (R_G - R_R) + (R_{L\downarrow} - R_{L\uparrow}) \quad (B1)$$

1145 Out of these four terms mentioned in eq.(B1), R_G and $R_{L\downarrow}$ are dependent on various factors such
 1146 as geographic location, season, cloudiness, aerosol loading, atmospheric water vapor content and
 1147 less on surface properties. On the other hand, the upwelling radiations in eq. (B1) strongly depends
 1148 on the surface properties such as surface reflectance and emittance, land surface temperature, and
 1149 soil water content (Zerefos and Bais, 2013).

1150 Instantaneous net radiation (R_{Ni}) can be derived using eq. B2 as follows (Mallick et al., 2007):

$$R_{Ni} = R_{ns} - R_{nl} \quad (B2)$$

$$R_{ns} = (1 - \alpha_R) R_G \quad (B3)$$

$$R_{nl} = R_{L\downarrow} - R_{L\uparrow} \quad (B4)$$

1151 Where, R_{ns} is net shortwave radiation ($W m^{-2}$), R_{nl} is net longwave radiation ($W m^{-2}$).and α_R is the
 1152 broadband surface albedo shortwave spectrum.

1153 A WMO (World Meteorological Organization) shortwave radiation model (Cano et al.,1986)
 1154 calibrated over Indian conditions (Mallick et al., 2007, 2009) was used to compute R_G using the
 1155 following equation:

$$R_G = \tau_{sw} G_{sc} E (\sin\beta_e)^{1.15} \quad (B5)$$

1156 Where, τ_{sw} is the is the global clear sky transmissivity for the shortwave radiation (0.7), G_{sc} is the
 1157 solar constant ($1367 Wm^{-2}$), ϵ is the eccentricity correction factor due to variation in Sun-Earth
 1158 distance and β_e is the sun elevation in degrees.

1159 $R_{L\downarrow}$ at any instance was calculated as follows:

$$R_{L\downarrow} = \epsilon_a \sigma (273.14 + T_A)^4 \quad (B6)$$

1160 Where, σ is the Stefan–Boltzmann constant ($5.67 \times 10^{-8} \text{ Wm}^{-2}\text{K}^{-4}$); T_A is the air temperature ($^{\circ}\text{C}$);
1161 ϵ_a is the atmospheric emissivity.

1162 Atmospheric emissivity (ϵ_a) was computed using the following equation (Bastiaanssen et
1163 al.,1998):

$$\epsilon_a = 0.85 - \ln\tau_{\text{sw}}^{0.09} \quad (\text{B7})$$

1164 $R_{L\uparrow}$ at any particular instance was calculated as follows:

$$R_{L\uparrow} = \epsilon_s \sigma (273.14 + T_s)^4 \quad (\text{B8})$$

1165 Where, ϵ_s is the surface emissivity in thermal infrared (8 – 14 μm) spectrum and T_s is the land
1166 surface temperature ($^{\circ}\text{C}$).

1167 **B2: Evaluation of STIC-TI R_{Ni}**

1168 Comparison of the clear-sky R_{Ni} estimates with respect to *in situ* measurements revealed RMSE in
1169 R_{Ni} to the order of 27 – 72 W m^{-2} , MAPD 8 –24%, BIAS (-67) – 50 W m^{-2} , and R^2 varying from
1170 0.62– 0.90 across all the sites (Fig. B2, Table B2). Among the nine sites, a consistent
1171 underestimation of R_{Ni} was noted in IND-Dha, US-Ton, and US-Var (with BIAS of -23 W m^{-2} , -
1172 61 W m^{-2} and -67 W m^{-2}), whereas substantial overestimation of R_{Ni} was found in IND-Sam, IND-
1173 Naw, and AU-ASM with a BIAS of 50 W m^{-2} , 37 W m^{-2} and 43 W m^{-2} , respectively (Table B2).

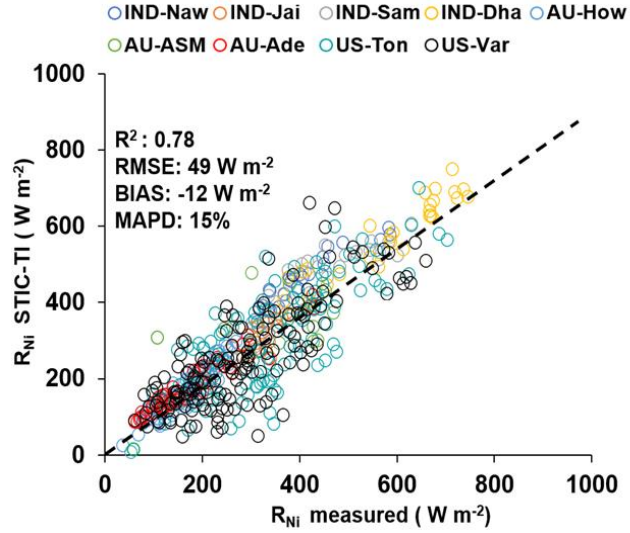


Figure B2: Validation of STIC-TI derived R_{Ni} estimates with respect to *in situ* measurements in different ecosystems. The regression equation between modeled versus in-situ R_{Ni} is, R_{Ni} (STIC-TI) = $0.78R_{Ni}$ (tower) + 58.92.

1174 **Table B2:** Performance evaluation statistics of clear-sky R_{Ni} estimates in nine different
 1175 agroecosystems

Sites	Error statistics of clear-sky R_{Ni} model estimates			
	R^2	BIAS ($W m^{-2}$)	RMSE ($W m^{-2}$)	MAPD (%)
IND-Jai	0.81	-9	32	8
IND-Naw	0.81	37	56	12
IND-Dha	0.81	-23	42	9
IND-Sam	0.64	50	67	15
US-Ton	0.68	-61	69	21
US-Var	0.62	-67	72	24
Au-How	0.87	7	27	15
AU-ASM	0.88	43	50	14
AU-Ade	0.90	11	27	16

1176 **Appendix C**

1177 **C1: Estimating SEB fluxes using STIC1.2 analytical model and thermal remote sensing data**

1178 STIC1.2 (Mallick et al., 2014, 2015a,b, 2016, 2018a) is a one-dimensional physically based SEB
1179 model and is based on the integration of satellite LST observations into the Penman–Monteith
1180 Energy Balance (PMEB) equation (Monteith, 1965). In STIC1.2, the vegetation–substrate
1181 complex is considered as a single unit. Therefore, the aerodynamic conductances from individual
1182 air-canopy and canopy-substrate components is regarded as an ‘effective’ aerodynamic
1183 conductance (g_A), and surface conductances from individual canopy (stomatal) and substrate
1184 complexes is regarded as an ‘effective’ canopy-surface conductance (g_S) which simultaneously
1185 regulate the exchanges of sensible and latent heat fluxes (H and LE) between surface and
1186 atmosphere. One of the fundamental assumptions in STIC1.2 is the first order dependence of these
1187 two critical conductances on M through T_S . Such an assumption enabled an integration of satellite
1188 LST in the PMEB model (Mallick et al., 2016). The common expression for LE and H according
1189 to the PMEB equation is as follows:

$$LE = \frac{s\phi + \rho c_P g_A D_A}{s + \gamma \left(1 + \frac{g_A}{g_S}\right)} \quad (C6)$$

$$H = \frac{\gamma\phi \left(1 + \frac{g_A}{g_S}\right) - \rho c_P g_A D_A}{s + \gamma \left(1 + \frac{g_A}{g_S}\right)} \quad (C7)$$

1190 In the above equations, the two biophysical conductances (g_A and g_S) are unknown and the
1191 STIC1.2 methodology is based on finding analytical solutions for the two unknown conductances
1192 to directly estimate LE (Mallick et al., 2016, 2018a). The need for such analytical estimation of
1193 these conductances is motivated by the fact that g_A and g_S can neither be measured at the canopy
1194 nor at larger spatial scales, and there is no universally agreed appropriate model of g_A and g_S that
1195 currently exists (Matheny et al., 2014; van Dijk et al., 2015). By integrating T_S with standard SEB
1196 theory and vegetation biophysical principles, STIC1.2 formulates multiple state equations in order

1197 to eliminate the need to use the empirical parameterizations of the g_A and g_S and also to bypass the
 1198 scaling uncertainties of the leaf-scale conductance functions to represent the canopy-scale
 1199 attributes. The state equations for the conductances are expressed as a function of those variables
 1200 that are mostly available as remote sensing observations and weather forecasting models. In the
 1201 state equations, a direct connection to T_S is established by estimating M as a function of T_S . The
 1202 information of M is subsequently used in the state equations of conductances, aerodynamic
 1203 variables (aerodynamic temperature, aerodynamic vapor pressure), and evaporative fraction,
 1204 which is eventually propagated into their analytical solutions. M is a unitless quantity, which
 1205 describes the relative wetness (or dryness) of a surface and also controls the transition from
 1206 potential to actual evaporation; which implies $M \rightarrow 1$ under saturated surface conditions and $M \rightarrow 0$
 1207 under extremely dry conditions. Therefore, M is critical for providing a constraint against which
 1208 the conductances are estimated. Since T_S is extremely sensitive to the surface moisture variations,
 1209 it is extensively used for estimating M in a physical retrieval scheme (detail in Appendix A3 of
 1210 Bhattarai et al., 2018; Mallick et al., 2016, 2018a). It is hypothesized that linking M with the
 1211 conductances will simultaneously integrate the information of T_S into the PMEB model. To
 1212 illustrate, we express the state equations by symbols, $sv_1 = f \{c_1, c_2, c_3, v_1, v_2, v_3, v_4, sv_3, sv_5\}$; sv_2
 1213 $= f \{v_4, sv_1, sv_5, sv_6\}$; $sv_3 = f \{c_3, v_3, v_4, sv_4, sv_5\}$; $sv_4 = f \{c_3, v_3, sv_1, sv_2, sv_7, sv_8\}$. Here, f , sv , v ,
 1214 and c denote the function, state variables, input variables (5 input variables; radiative and
 1215 meteorological), and constants (3 constants), respectively. Here sv_1 to sv_4 are g_A , g_S , aerodynamic
 1216 temperature (T_0), evaporative fraction (Λ), and sv_8 is M . Given the estimates of M , net radiative
 1217 energy ($R_{N_i} - G_i$), T_A , R_H , the four state equations are solved simultaneously to derive analytical
 1218 solutions for the four state variables and to produce a surface energy balance “closure” that is
 1219 independent of empirical parameterizations for g_A , g_S , T_0 , and Λ . However, the analytical solutions
 1220 to the four state equations contain three accompanying unknown state variables (effective vapor
 1221 pressures at source/sink height, and Priestley-Taylor variable), and as a result there are four
 1222 equations with seven unknowns. Consequently, an iterative solution was found to determine the
 1223 three additional unknown variables as detailed in this section above and also described in Mallick
 1224 et al. (2016, 2018a) and Bhattarai et al. (2018). The state equations of STIC are given below.

$$g_A = \frac{\phi}{\rho_{CP} \left[(T_0 - T_A) + \left(\frac{e_0 - e_A}{\gamma} \right) \right]} \quad (C1)$$

$$g_S = g_A \frac{(e_0 - e_A)}{(e_0^* - e_0)} \quad (C2)$$

$$T_0 = T_A + \left(\frac{e_0 - e_A}{\gamma} \right) \left(\frac{1 - \Lambda}{\Lambda} \right) \quad (C3)$$

$$\Lambda = \frac{2\alpha s}{2s + 2\gamma + \gamma \frac{g_A}{g_S} (1 + M)} \quad (C4)$$

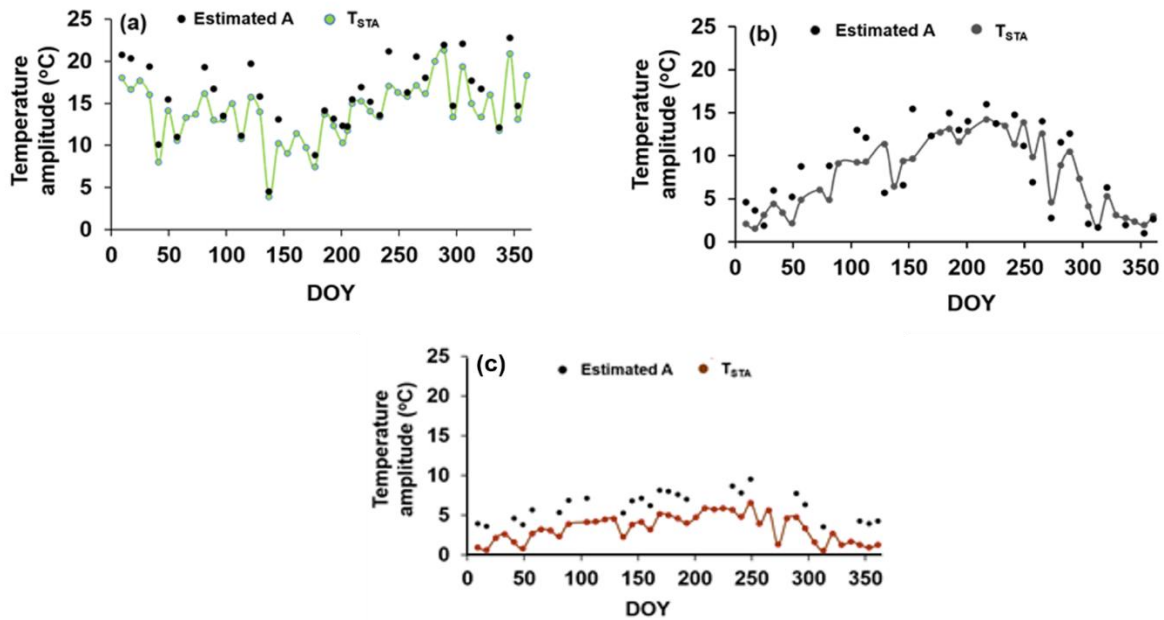
1225 Detailed derivations of these four state equations are given in Mallick et al. (2016). Given the
 1226 values of M , R_N , G , T_A , and R_H or e_A , the four state equations can be solved simultaneously to
 1227 derive analytical solutions for the four unobserved variables and to simultaneously produce a
 1228 ‘closure’ of the PMEB model that is independent of empirical parameterizations for both g_A and
 1229 g_S . However, the analytical solutions to the four state equations contain three accompanying
 1230 unknowns; e_0 (vapor pressure at the source/sink height), e_0^* (saturation vapor pressure at the
 1231 source/sink height), and Priestley-Taylor coefficient (α), and as a result there are four equations
 1232 with seven unknowns. Consequently, an iterative solution was needed to determine the three
 1233 unknown variables (as described in Appendix A2 in Mallick et al. 2016). Once the analytical
 1234 solutions of g_A and g_S are obtained, both variables are returned into eq. (13) to directly estimate
 1235 LE.

1236 In STIC-TI, an initial value of α was assigned as 1.26; initial estimates of e_0^* were obtained from
 1237 T_s through temperature-saturation vapour pressure relationship, and initial estimates of e_0 were
 1238 obtained from M as, $e_0 = e_A + M(e_0^* - e_A)$. Initial T_{0D} and M were estimated according to
 1239 Venturini et al. (2008) as described in section 3.2, and initial estimation of G was performed from
 1240 initial M using the equation sets eq. (2) – eq. (11). With the initial estimates of these variables;
 1241 first estimate of the conductances, T_0 , Λ , H , and LE were obtained. The process was then iterated
 1242 by updating e_0^* , D_0 , e_0 , T_{0D} , M , and α (using eq. A9, A10, A11, A17, A16 and A15 in Mallick et
 1243 al., 2016), with the first estimates of g_S , g_A , T_0 , and LE, and re-computing G , ϕ , g_S , g_A , T_0 , Λ , H ,
 1244 and LE in the subsequent iterations with the previous estimates of e_0^* , e_0 , T_{0D} , M , and α until the

1245 convergence of LE was achieved. Stable values of G, conductances, LE, H, T_0 , e_0^* , e_0 , T_{0D} , M, and
1246 α were obtained within ~25 iterations. The inputs needed for computation of LE_i (eq.C6) are air
1247 temperature (T_A), land surface temperature (T_S), relative humidity (R_H), net radiation (R_{Ni}) and
1248 soil heat flux (G_i).

1249 Appendix D

1250 The temporal variation of estimated A and T_{STA} is shown in Fig. D1. The annual variations of T_{STA}
1251 in different ecosystem was found to be within the ranges of 1 - 4° C.



1252
1253 **Figure D1:** Temporal variation of A and T_{STA} in (a) AU-ASM (2013), (b) US-Ton (2014), (c) US-
1254 Var (2014).

1255

1256

1257

1258

1259

1260

1261

1262 **Appendix E**

1263 **Table E1:** Soil textural properties and their values used in the present study (Murray and Verhoef,
 1264 2007; Minasny et al., 2011; Anderson et al., 2007)

Soil texture	Water retention Shape parameter (δ)	Field capacity (vol/vol) (%) θ_{fc}	Wilting point (vol/vol) (%) θ_{wp}	Sand fraction (f_s)	Saturated soil moisture (vol/vol) (%) θ^*
Sand	2.77	10	5	0.92	43
Loamy Sand	2.39	12	5	0.82	41
Sandy loam	2.27	18	8	0.58	41
Loam	2.20	28	14	0.43	43
Silty loam	2.22	31	11	0.17	45
Sandy clay loam	2.17	27	17	0.58	39
Clay loam	2.14	36	22	0.40	41
Silty clay loam	2.14	38	22	0.10	43
Sandy clay	2.11	36	25	0.52	38
Silty clay	2.12	41	27	0.06	46
Clay	2.10	42	30	0.22	38

1265 **Appendix F**

1266 [Day-night view angle effect on errors of STIC-TI heat flux estimates from measurements is shown](#)
1267 [in Figure F.](#)

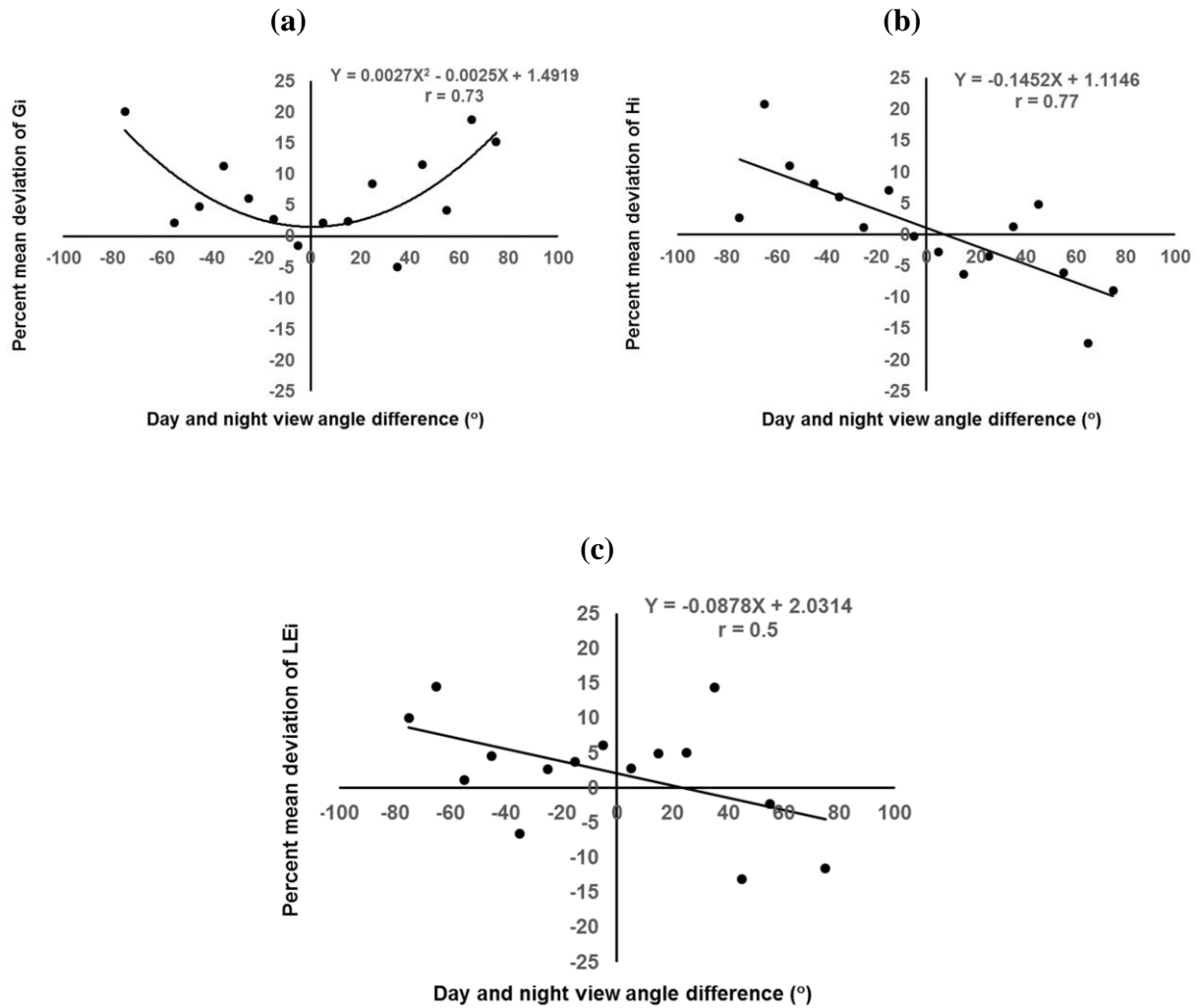


Figure F: [Dependence of STIC-TI model flux error in terms of mean percent deviation from measurements on day-night view angle difference of MODIS Aqua expressed as mean of 10° bin for \(a\) \$G_i\$, \(b\) \$H_i\$, and \(c\) \$LE_i\$ fluxes.](#)

1268

1269

1270